Experimental investigation of the residues produced in the ^{136}Xe + Pb and ^{124}Xe + Pb fragmentation reactions at 1A GeV

D. Henzlova,[1,*,†,‡] K.-H. Schmidt,[1] M. V. Ricciardi,[1] A. Kelić,[1] V. Henzl,[1,*] P. Napolitani,[1,2,3] L. Audouin,[2] J. Benlliure,[4] A. Boudard,[5] E. Casarejos,[4] J. E. Ducret,[5] T. Enqvist,[6] A. Heinz,[7] A. Junghans,[8] B. Jurado,[9] A. Krása,[10] T. Kurtukian,[4] S. Leray,[5] M. F. Ordóñez,[4,§] J. Pereira,[4,*] R. Pleskač,[1] F. Rejmund,[11] C. Schmitt,[12] C. Stéphan,[2] L. Tassan-Got,[2] C. Villagrasa,[5] C. Volant,[5] A. Wagner,[8] and O. Yordanov[1,‖]

[1]*GSI, Planckstraße 1, D-64291 Darmstadt, Germany*
[2]*IPN Orsay, IN2P3, F-91406 Orsay, France*
[3]*LPC Caen, Université de Caen, CNRS/IN2P3, ENSICAEN, Caen, France*
[4]*University of Santiago de Compostela, E-15706 Santiago de Compostela, Spain*
[5]*DAPNIA/SPhN CEA/Saclay, F-91191 Gif-sur-Yvette, France*
[6]*CUPP Project, P. O. Box 22, FI-86801, Pyhäsalmi, Finland*
[7]*Wright Nuclear Structure Laboratory, Yale University, New Heaven, Connecticut 06520, USA*
[8]*Forschungszentrum Rossendorf, D-01314 Dresden, Germany*
[9]*CENBG, IN2P3, F-33175 Gradignan, France*
[10]*Nuclear Physics Institute, CZ-25068 Řež, Czech Republic*
[11]*GANIL, F-14076 Caen, France*
[12]*Université Lyon I, CNRS/IN2P3, IPNL, Rue Enrico Fermi, F-69622 Villeurbanne, France*

The nuclide cross sections and longitudinal velocity distributions of residues produced in the reactions of ^{136}Xe and ^{124}Xe at 1A GeV in a lead target were measured at the high-resolution magnetic spectrometer, the fragment separator (FRS) of GSI. The data cover a broad range of isotopes of the elements between $Z = 3$ and $Z = 56$ for ^{136}Xe and between $Z = 5$ and $Z = 55$ for ^{124}Xe, reaching down to cross sections of a few microbarns. The velocity distributions exhibit a Gaussian shape for masses above $A = 20$, while more complex behavior is observed for lighter masses. The isotopic distributions for both reactions preserve a memory on the projectile N/Z ratio over the whole residue mass range.

PACS number(s): 25.70.Mn, 25.60.Gc, 21.10.Ft, 21.65.Cd

I. INTRODUCTION

Heavy-ion collisions, being an ideal tool for producing hot nuclear matter at various densities in the laboratory, are an important source of information on the properties of nuclear matter under extreme conditions. Experimental studies in this field extend from the Fermi energy regime to relativistic energies. These two energy regimes are characterized by quite different types of reaction dynamics. If the projectile velocity is comparable to the Fermi velocity, nucleon exchange between the reaction partners during the collision is important. During the collision stage, the neutron-to-proton ratio N/Z of projectile and target tends to equilibrate. Observation of the magnitude of this process (known as isospin diffusion) carries information on the symmetry energy coefficient at high temperature and density [1,2]. Noncentral collisions at these energies are characterized by deep-inelastic transfer [3], while

central collisions form a highly excited compressed piece of nuclear matter, suitable for the study of multifragment decay and phase transitions [4].

At relativistic energies, the Fermi spheres of projectile and target are well separated. Transfer of nucleons is very unlikely, and the geometrical abrasion picture seems well justified [5]. Flow patterns of nucleons and particles as well as kaon production from central collisions have been studied to deduce the equation of state of hot and compressed nuclear matter [6,7]. At larger impact parameters, spectator matter is sheared off from the projectile and target and continues moving essentially with its original velocity. A considerable amount of excitation energy [8] and a slight momentum transfer [9] are induced, but compression is small. Therefore, peripheral heavy-ion collisions provide an ideal scenario for studying multifragment decay of hot and dilute nuclei [10], avoiding additional dynamical effects due to compression, which are important, e.g., in central heavy-ion collisions at Fermi energies.

Most experimental devices, developed for such studies, aim for covering the full solid angle in order to provide a complete survey on multiplicities and correlations of charged-particle production. Although this information is crucial for many conclusions, high-precision information on mass and momentum is lacking, since the resolution of these devices is rather limited. This is particularly unsatisfactory if the evolution of the N/Z degree of freedom is to be studied.

---

*Present address: NSCL-MSU, 1 Cyclotron, East Lansing, MI 48824, USA.

†This work forms part of the Ph.D. thesis of Daniela Henzlova.

‡Corresponding author: henzlova@nscl.msu.edu

§Present address: CIEMAT, Avda. Complutense 22, 28040 Madrid, Spain.

‖Present address: INRNE, 72 Tzarigradsko chaussee, BG-1784 Sofia, Bulgaria.

To study the effects of "isospin diffusion," systematic studies on the isotopic distributions of heavy nuclei from heavy-ion collisions at Fermi energies have been performed with high-resolution spectrometers, e.g. [8], using projectiles and targets with different neutron excess. However, the situation after the collision stage is not directly observable, because it is further modified by sequential and eventually multifragment decay. Consequently, the final observed isotopic distributions carry the combined information from both: collision and decay stage of the reaction. On the other hand, the isotopic distributions of heavy nuclei from relativistic heavy-ion collisions, where nucleon exchange during the collision is negligible, can give more direct insight into the influence of sequential decay and eventually multifragment decay on the N/Z degree of freedom. Therefore, by combining the experimental results from the two energy regimes, one can gain more specific information on the evolution of the N/Z degree of freedom during the different stages of the reaction.

Moreover, high-resolution experiments on heavy-ion collisions at relativistic energies can provide deeper insight into the thermal properties of highly excited nuclear systems and on possible liquid-gas phase transitions [9,10]. Detailed study of the kinematics of the spectator matter has also revealed information on the nonlocal properties of the nuclear force [11,12].

Unfortunately, detailed experimental information on heavy residue production in heavy-ion collisions at relativistic energies is rather lacking. Using the heavy-ion accelerator SIS18 at GSI, an experimental campaign on the formation of heavy residues by spallation reactions of heavy projectiles in hydrogen and deuterium targets has been performed. This campaign, which was motivated by nuclear technology, has demonstrated the power of the experimental method and has provided a systematic set of high-quality data [13]. However, by using heavier targets, considerably higher excitation energies can be introduced in the collision. Therefore, extending experimental investigations toward heavy-ion collisions at relativistic energies may appreciably broaden our knowledge on the properties of highly excited nuclei.

The present work is dedicated to the first experiment on determining the full nuclide distributions of projectile-like residues in two systems with very different N/Z content: ^{124}Xe and ^{136}Xe + Pb, at the beam energy of $1A$ GeV. The heavy target nucleus has been chosen to minimize the surface that divides the projectile spectator from the participant zone for a given size of the projectile spectator. Thus, surface effects due to the abrasion process should be minimized. The experiment has been performed at the magnetic spectrometer FRS at GSI. Because of its high resolution, all residues were identified in mass number A and nuclear charge Z. Moreover, the longitudinal momenta of all residues were determined with high precision.

The present paper explores the isotopic composition of the final residues measured in a broad range of nuclear charge and the influence of the neutron-to-proton ratio of the initial system on the isotopic composition of the final residues. Results on high-resolution measurements of longitudinal residue velocities are also given. This paper is dedicated to presenting the experimental data. More detailed discussions
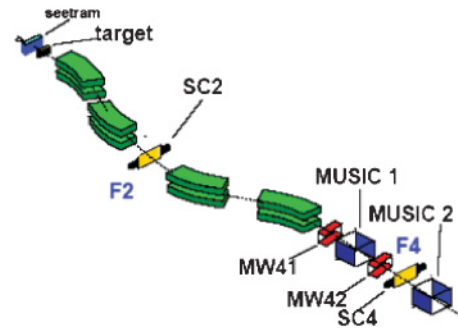

FIG. 1. (Color online) Schematic view of the FRS and the associated detector equipment.

and comparisons with nuclear-reaction models will be the subjects of forthcoming publications.

II. EXPERIMENTAL TECHNIQUE

The experiments with the two xenon beams, ^{124}Xe and ^{136}Xe, both at $1A$ GeV, were performed at the fragment separator (FRS) at GSI. The beams were delivered by the heavy-ion synchrotron (SIS) with intensities of $\sim 3 \times 10^8$ and $\sim 4 \times 10^7$ particles per spill for ^{124}Xe and ^{136}Xe, respectively. In both experiments, the spill length was varied between 1 and 10 s to keep the maximum counting rate allowed by the detector limits and the data acquisition system. In the following, the principles of the isotopic identification at the fragment separator and its detection system will be described.

The FRS [13] is a high-resolution magnetic spectrometer, which allows mass and element separation of the final residues ranging from the lightest masses up to the mass of the heavy projectile. The projectile-like fragments exiting the target are detected and isotopically identified in flight in the associated detector equipment. A schematic view of the experimental setup is shown in Fig. 1.

The FRS is a two-stage magnetic spectrometer with a maximum bending power of 18 Tm, an angular acceptance of 15 mrad around the beam axis, and a momentum acceptance of 3%. A beam monitor, the SEETRAM (secondary electron transmission monitor), was used to constantly measure the number of incoming beam particles. The beam monitor and its calibration system are mounted in front of the spectrometer [14–16]. The SEETRAM consists of three thin foils of 11.5 cm in diameter which are mounted perpendicular to the beam axis. The outer foils are made of 14 μm thin aluminum, while the middle foil is made of a 10 μm thin titanium layer. The reaction rate in the SEETRAM amounts to less than 0.1%, and the energy loss to less than 0.05% for both primary beams. The target is located 2.27 m in front of the first quadrupole of the FRS. In both experiments, a natural lead foil of 635 mg/cm^2 thickness was used as a target. The primary beam loses less than 2% of its energy in the lead target. Corrections due to energy loss thus do not deteriorate the accurate measurement of the longitudinal momenta of the reaction products.

The standard FRS detection equipment was used for the isotopic identification. It consists of two plastic scintillation detectors, two multiple-sampling ionization chambers

(MUSIC) [17] and a system of multiwire-proportional counters (MWPC) [18] located as shown in Fig. 1. To cover the full nuclear-charge range, the measurements performed in the present experiments were split into two groups of settings of the FRS. In the light-fragment settings, the fragments with charge $Z < 30$ were measured, while in the heavy-fragment settings, fragments with charge $Z > 25$ were detected in order to have a sufficient overlap of the measured cross sections. In the case of light-fragment settings, a degrader in the intermediate image plane was used so that only the fragments up to $Z \sim 30$ were transmitted through the FRS. Moreover, because of the limited momentum acceptance of the FRS, fragments with a relatively narrow range of A/Z and/or velocities (i.e., magnetic rigidity $B\rho$) are transmitted in a given magnetic field. Thus, around 50 different settings of the magnetic fields had to be used within the light- and heavy-fragment FRS settings to measure the reaction products in a broad range of A/Z and/or velocities. The magnetic fields of the first two dipoles were changed in steps of 1.5%, and the fields of the last two dipoles were correspondingly adjusted to keep a selected nuclear charge on the central trajectory. A step of 1.5% was chosen, since it corresponds to half the FRS momentum acceptance, which ensures sufficient overlap of the velocity distributions measured in the neighboring settings. In this way, the full velocity distributions could be reconstructed with a high quality. Since the full momentum (velocity) distributions of all residues are reconstructed from measurements performed in several different magnetic-field settings, see Fig. 2, the limited acceptance in momentum does not affect the measured results. For each produced nuclide, the integral of its velocity distribution, normalized to the number of beam particles, is evaluated to determine the production cross section.

Because of the limited angular acceptance of the FRS, the transmission of residues having broad angular distributions is reduced and thus also the measured yields. While the heavy residues are produced with rather narrow angular distributions and they are almost fully transmitted through the FRS, the angular distributions of light residues are rather broad, and
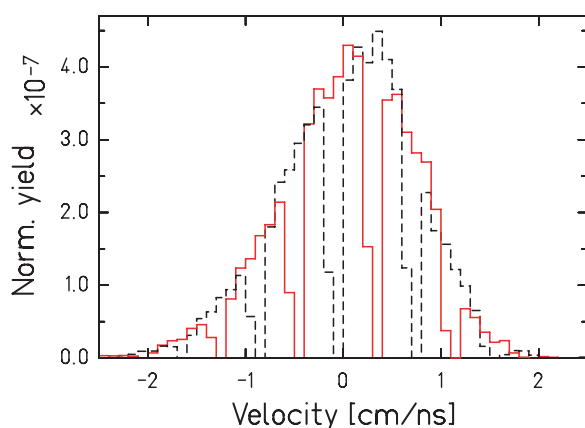

FIG. 2. (Color online) Velocity distribution of the isotope ^{31}P measured in the ^{136}Xe + Pb experiment. Different parts of this distribution measured in neighboring settings of the magnetic fields are marked by full and dashed histograms.

the angular transmission of these residues may be as low as 10%. As discussed later, the rather low transmission of the light residues may nevertheless be corrected for, using a dedicated transmission calculation [19], which simulates the transmission of every ion species through the magnetic fields of the FRS.

III. DATA ANALYSIS

The identification of the residues is the key part of the data analysis. In the following, the main steps of the analysis are outlined. A more detailed description of the analysis procedure can be found in Ref. [20]. To determine the mass of the final residue, its charge, velocity, and magnetic rigidity must be known. The mass identification is then performed according to the relation

$$\frac{A}{q} = \frac{e}{u} \frac{B\rho}{\beta\gamma c}. \tag{1}$$

Here, e is the magnitude of the electron charge, u is the atomic mass unit, γ represents the relativistic Lorentz factor $\gamma = \sqrt{(1-\beta^2)^{-1}}$ with $\beta = v/c$, c is the speed of light, and q corresponds to the ionic charge of the fragment.

On the passage through various layers of matter in the beamline, the produced fragments may catch or lose electrons. These processes depend on the velocity of the fragments, the velocity of the electrons in their orbits, and the material of the layer of matter. Ions with different charge states follow different trajectories in the FRS. This change of trajectory of the ion in the magnetic field following the capture or loss of an electron was used to separate the charge states of the final residues and to remove the majority of incompletely stripped ions from the analysis [21]. Nevertheless, a small fraction of incompletely stripped ions, which cannot be identified this way, still remains and may contaminate the cross sections of completely stripped ions. In the case of both investigated reactions, this contribution was well below 1% for all the residues. Thus, in the following, only residues with $q = Z$ are considered to enter the above equation.

The velocity of every residue is determined from the measurement of its time-of-flight (TOF) using the relation $v = l/\text{TOF}$, where l is the length of the flight path of the residue. To determine the fragment velocity, its TOF is measured between the scintillation detectors located in the intermediate dispersive and final achromatic image planes F2 and F4 (see Fig. 1), respectively, over the flight path of 36.8 m. The resolution of the TOF determination is given by the time resolution of the scintillation detectors and is as good as 100 ps (full width at half maximum, FWHM). This allows us to determine the velocity parameter $\beta\gamma$ with a relative uncertainty of 2.8×10^{-3}.

Since the time-of-flight measurement is performed over the second stage of the Fragment Separator, the magnetic rigidity $B\rho_{II}$ of every residue in the last two dipoles of the FRS must be determined for use in Eq. (1). The determination of the magnetic rigidity consists of the measurement of the radius of the fragment trajectory in the second stage of the FRS for a given magnetic field. The value of the magnetic field

is measured by Hall probes, and the radius of the trajectory is determined by measuring the fragment positions in two scintillation detectors situated at the final achromatic (F4) and intermediate dispersive (F2) image planes, respectively. The resolution in magnetic rigidity is given by the ion-optical properties of the FRS and by the position resolution of the scintillation detectors and is as high as $\Delta B\rho/(B\rho) = 5 \times 10^{-4}$ (FWHM).

Apart from velocity and magnetic rigidity, also the nuclear charge of every residue must be known in order to perform the mass identification according to Eq. (1). To measure the charge of the produced fragments, two multiple-sampling ionization chambers located at F4 behind the scintillation detector were used. To obtain the nuclear charge of the residue with high resolution, several corrections must be applied to the measured energy-loss signal. The final, corrected energy loss reads

$$\Delta E_{\mathrm{corr}} = \Delta E_{\mathrm{meas}} \, f_1(v) \, f_2(x) \, f_3(T, p), \qquad (2)$$

where $f_1(v)$ is a correction for the velocity dependence of the energy loss, $f_2(x)$ is used to correct for the dependence of the energy-loss signal on the horizontal position in the final image plane, and $f_3(T, p)$ is a correction for the change of pressure and temperature in the ionization chamber. A more detailed description of these corrections may be found in Ref. [21].

A. Mass and nuclear-charge identification

Once fully stripped ions are selected, their mass and nuclear charge may be identified. The easiest way to obtain the identification is to display the energy-loss signals measured by the MUSIC versus the A/Z ratio calculated using Eq. (1).
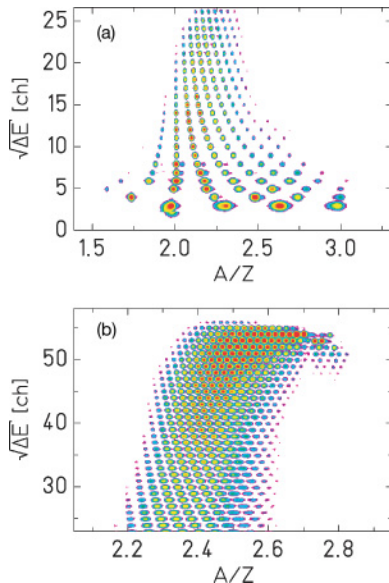
In Fig. 3, the identification plots from the ^{136}Xe + Pb experiment as measured in the light- and heavy-fragment settings are shown. Each single spot in the figure corresponds to an individual fragment of a given mass A and a nuclear charge Z. The high resolution in mass and nuclear charge achieved in this experiment may be seen in the clear separation of the spots corresponding to different nuclides. The mass resolving power, defined by the resolution of the measurements of magnetic rigidity ($B\rho$) and TOF, corresponds to $A/\Delta A \approx 400$ even for the heaviest residues. The resolution of the nuclear charge is as good as $\Delta Z = 0.4$ units (FWHM) for all residues. This allows us to isotopically identify all the reaction products ranging from the lightest ones up to the heavy projectile. A regular pattern may be observed in the positions of the single nuclides: the fragments to the right of the $A/Z = 2$ chain [Fig. 3(a)] correspond successively to isotopes with $N = Z + 1, Z + 2$, etc.; while fragments to the left correspond to $N = Z - 1, Z - 2$ etc. This pattern continues in the heavy-fragment settings. The mass and charge identification may now be easily performed using the known A and Z of the particle-unstable nuclei, i.e., ^{8}Be, ^{9}B, and ^{16}F and the regular pattern of $N = Z + k(k = -2, -1, \ldots)$.

The regular pattern and the known A, Z of the projectile may be used to extend the identification toward heavy residues. In this way, a unique identification both in nuclear charge and mass may be performed. Note that the slight deviation of $A/Z = 2$ from a strictly vertical line, observed in Fig. 3(a), does not affect the result of the nuclide identification, after which every fragment is fully specified in A and Z as integer numbers. The validity of the identification of single nuclides is confirmed by a correct "overlap" of the mass and nuclear charge distributions as well as of $\langle N \rangle/Z$ determined in the light and heavy datasets. The isotopes of $Z = 3$ were the lightest residues detected and identified in the ^{136}Xe + Pb experiment.

Similar considerations were applied for the identification of residues from the ^{124}Xe + Pb experiment, and the

FIG. 3. (Color online) Identification plots from the ^{136}Xe + Pb experiment: (a) light-fragment settings; (b) heavy-fragment settings. The vertical scale corresponds approximately to the atomic number Z.
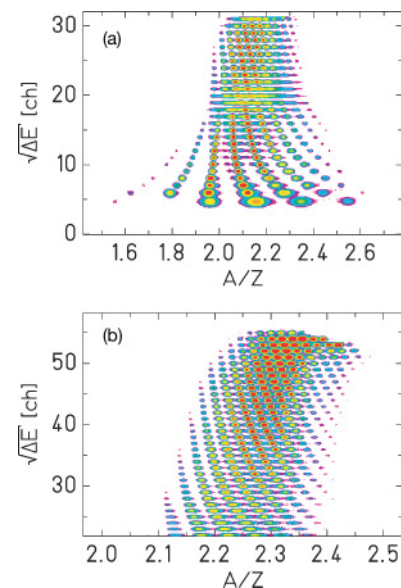

FIG. 4. (Color online) Same as Fig. 3, but from the ^{124}Xe + Pb experiment.

corresponding identifications plots are shown in Fig. 4. In this experiment, the lowest nuclear charge measured was $Z = 5$. Also in this experiment, a high mass and nuclear-charge resolution was achieved, as may be seen in the clear separation of the spots corresponding to different nuclides.

From Fig. 4(a), a poor mass resolution may be observed in the range corresponding to nuclear charges $Z = 18$–22. This is a consequence of a malfunction of the constant-fraction discriminator used to obtain the position information from the arrival time of the signal from one side of the scintillation detector located in the intermediate image plane. Despite this, it was possible to reconstruct the isotopic identification and determine the production cross sections of the single isotopes by means of the time-of-flight measurement for all but the potassium isotopes, which had to be reconstructed using data measured in the heavy-fragment magnetic-field settings. The corresponding production cross sections of these isotopes, however, suffer from larger systematic uncertainty.

B. Determination of the production cross sections and velocity distributions

To determine the production cross sections from the measured yields of single nuclides, the following relation is used:

$$\sigma(N, Z) = \frac{Y_{\mathrm{meas}}(N, Z)}{N_{\mathrm{Pb}} T(N, Z)} s(A). \tag{3}$$

Here N_{Pb} is the number of lead-target nuclei per unit area, $Y_{\mathrm{meas}}(N, Z)$ stands for the dead-time-corrected production rate per incident projectile, $T(N, Z)$ represents the correction factor for the transmission losses due to the limited angular acceptance of the FRS, and $s(A)$ includes corrections for secondary interactions in the materials in the beamline.

After the identification of A and Z, the value of $\beta\gamma$ for each fragment was recalculated from the equation

$$\beta\gamma = \frac{e}{c} \frac{Z B \rho}{M(A, Z)}, \tag{4}$$

where $M(A, Z)$ is the mass of the nucleus (A, Z). In this way, the final resolution in the $\beta\gamma$ measurement is given only by the resolution in $B\rho$, since A and Z are integer numbers after identification; therefore, the resolution is improved by almost an order of magnitude over the resolution obtained from the TOF measurement. To obtain the correct shape of the velocity distribution, the number of counts measured in each magnetic-field setting was normalized to the number of beam ions impinging on the target in this setting. Finally, the velocity distributions from single settings were combined, and the full velocity distribution as illustrated in Fig. 2 for ^{31}P was obtained.

The yields obtained by the integration of these velocity distributions still need to be corrected for the limited angular acceptance of the FRS. For this purpose, the transmission calculation developed in Ref. [19] was applied. The model is based on the assumption that momentum distributions have an isotropic Gaussian shape around the mean value of the momentum of the emitting source. Using this calculation, the transmission coefficients were determined. The importance of the transmission correction decreases with increasing nuclear charge of the residue, since heavier residues are produced with narrower angular distributions, and the angular acceptance of the FRS is adapted to the emittance of heavy fragmentation products. In both experiments, the transmission $T(N, Z)$ varied between 25% for $Z \sim 10$ and reached 100% for $Z \sim 40$. The uncertainty of the transmission correction decreases with increasing nuclear charge and varies between 9% for $Z = 10$ and below 1% for $Z > 33$.

The correction for secondary reactions in the materials in the FRS beamline (scintillation detector, degrader) was performed using calculations [22,23] based on the Glauber approach. The corrections range from 3% for $A = 5$ to 10% for $A = 60$ for light-fragment settings and from 6% for $A = 50$ to 10% for $A = 136$ for heavy-fragment settings. The higher correction values for of light-fragment settings are caused by the thick degrader, which was not used in the heavy-fragment settings. The uncertainty of the secondary-reaction calculation corresponds to about 10%, which results in a relative systematic uncertainty of production cross sections between 0.3–1% for $A = 5$–60 and 0.6–1% for $A = 50$–136. The contribution of the secondary reactions in the target material does not exceed 1% for all measured fragments.

IV. EXPERIMENTAL RESULTS

In this section, the experimental results concerning isotopic, mass, and nuclear-charge distributions as well as velocity distributions of the residues formed in the reactions of ^{124,136}Xe + Pb at $1A$ GeV will be presented.

A. Velocity distributions

The approach, outlined above, to determine the full velocity distributions inside the angular acceptance of the FRS was applied for both measured systems, and examples of some velocity distributions are shown in Fig. 5.

For most residues, the longitudinal velocity distributions show Gaussian-like shapes. The tendencies observed in the upper mass range agree with those expected from systematics [24]: the width increases and the mean value decreases with decreasing mass. The width reveals the influence of the Fermi momenta of the abraded nucleons [25] as well as the influence of particle evaporation from the thermally equilibrated system [26], while the mean value reflects the friction experienced by the projectile spectator in the abrasion process. The influence of the Fermi momenta and evaporation on the width of the velocity distribution can be well demonstrated by comparing velocity distributions of ^{123}Xe produced from ^{124}Xe and ^{136}Xe projectiles, respectively. While in the latter case ^{123}Xe is produced by an abrasion and evaporation of 13 nucleons, resulting thus in relatively broad velocity distribution, the width of the distribution gets considerably narrower in the case of ^{124}Xe projectile due to an abrasion of a single nucleon only.

For elements below magnesium, the longitudinal velocity distributions become more complex and deviate from a Gaussian shape. Between neon and carbon, they are asymmetric
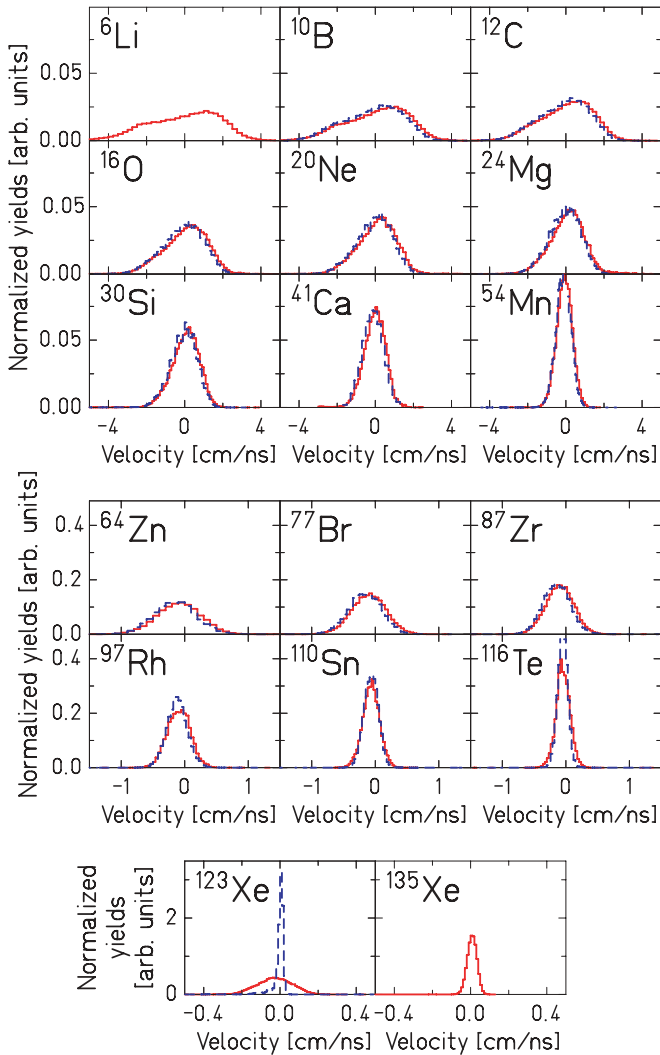
FIG. 5. (Color online) Measured longitudinal velocity distributions in the projectile frame for several nuclides measured in the ^{136}Xe + Pb (full red histogram) and the ^{124}Xe + Pb (dashed blue histogram) experiments. Note the different horizontal scales for different subgroups of data.

with a tail to lower velocities. For lithium, a second peak even develops at low velocities. Complex structures in the velocity distributions have been observed previously for the light residues of the systems ^{56}Fe+^{1}H, Ti [27] from another experiment at the FRS. In ^{56}Fe+^{1}H, the lightest residues showed double-humped distributions, typical of binary asymmetric mass splits. In contrast, the system ^{56}Fe + Ti showed Gaussian-like distributions over the whole mass range. This would be compatible with assuming multifragmentation as the dominant production mechanism for the lightest residues in reactions with the heavier titanium target. These results show that fragments of the same size can be produced by different reaction mechanisms. This observation suggests that the present data may be interpreted as a manifestation of different mechanisms resulting in the production of a given fragment in the same system. However, a more detailed discussion on this subject, which requires performing dedicated model

calculations with a suitable nuclear-reaction code, is beyond the scope of the present paper and will be the subject of a forthcoming paper.

In the following discussion, it is assumed that in the projectile frame of reference, the velocity distributions of the residues with atomic numbers larger than 9 are well represented by three-dimensional Gaussian distributions, which are isotropic in velocity space and centered at a mean value that is slightly lower than the beam velocity. Under this condition, the losses due to the limited angular acceptance of the FRS can be estimated using the algorithm of Ref. [19]. For the lighter residues having the asymmetric velocity distributions, only the directly measured production cross sections inside the angular acceptance of the FRS will be given.

B. Angular-acceptance-integrated production cross sections

To provide the full isotopic distributions over a broad range of elements, the production cross sections over several orders of magnitude had to be measured. An overview of the complete dataset laid over the chart of nuclides is shown in Fig. 6. Several missing isotopes may be noted in the vicinity of the ^{124}Xe projectile. The velocity distributions of these isotopes (for their N and Z see Table I in the Appendix) in the case of ^{124}Xe + Pb were severely cut by slits, which were inserted to protect the detectors from the most intense charge states of the primary beam with zero, one, and two electrons, and thus their cross sections could not be recovered.

The angular-acceptance-integrated production cross sections (not corrected for the limited angular acceptance of the FRS affecting mainly lighter residues) were determined for isotopes of elements $Z = 5$–55 and $Z = 3$–56 in the ^{124}Xe + Pb and the ^{136}Xe + Pb experiments, respectively. The angular-acceptance-integrated cross section σ_{acc} may be expressed as

$$\sigma_{\text{acc}} = \int_0^{\alpha_{\text{FRS}}} \frac{d\sigma}{d\alpha} d\alpha, \tag{5}$$

where α_{FRS} denotes the FRS acceptance of 15 mrad around the beam axis. The interest in the angular-acceptance-integrated cross sections lies in the fact that they provide directly measured quantities independent of the assumptions on the velocity distributions in the full velocity space needed to model the transmission of fragments through the FRS and on the transmission calculation itself. Since the velocity distributions of the fragments from both reactions are similar, the angular-acceptance-integrated isotopic distributions are well suited for the relative comparison of the products of the two reactions. The numerical values of the transmission-corrected production cross sections for both experiments are listed in the Appendix.

The angular-acceptance-integrated isotopic distributions from both experiments measured in the nuclear-charge range $Z = 5$–55 (^{124}Xe + Pb) and $Z = 3$–56 (^{136}Xe + Pb) are compared in Figs. 7–9. The cross sections measured in both experiments extend over a range of ≈ 1 μb to 2b with the production cross sections for the isotopes of a single element spanning in most cases over three orders of magnitude. Because of the thresholds of the electronics, some losses
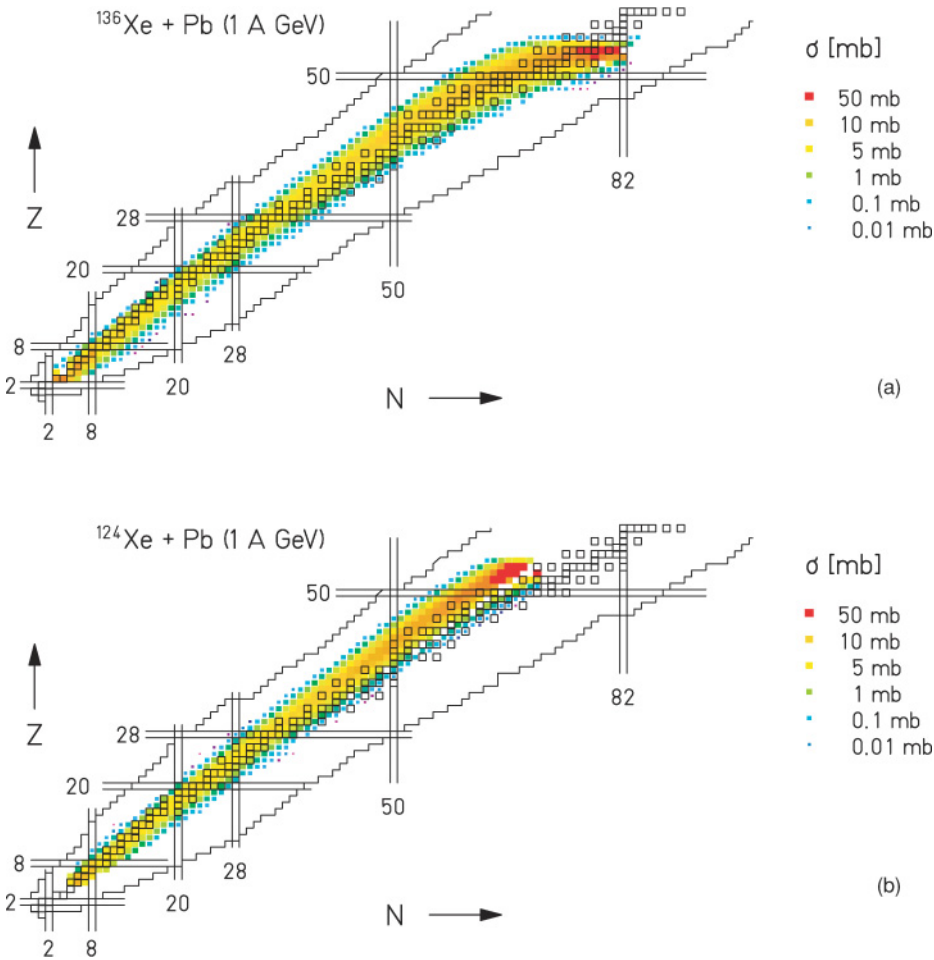
FIG. 6. (Color online) Angular-acceptance-integrated production cross sections for isotopes of elements $Z = 3$–56 and $Z = 5$–55 measured in the ^{136}Xe + Pb and ^{124}Xe + Pb experiments, respectively, presented on the chart of nuclides. Missing isotopes close to the projectile in the ^{124}Xe + Pb chart are due to more restrictive slit settings in this experiment (see the text).

may be expected in case of $Z = 3$ isotopes measured in the ^{136}Xe + Pb experiment, and the corresponding cross sections introduced in Fig. 7 should be considered as lower limits only. Please, note that not all the isotopes visible in the identification pattern in Figs. 3 and 4 may be found in Figs. 7–9. For the lightest residues, this is due to their broad velocity distributions, which were not fully measured for all the detected isotopes, and thus the cross section could not be properly determined. Similar to the case of the ^{124}Xe projectile, several heavy neutron-rich isotopes from ^{136}Xe experiment ($48 \leqslant Z \leqslant 52$), were affected by the setting of slits resulting in the apparent deviation of the corresponding cross sections from a smooth trend.

Several interesting observations can be made by comparing the shapes of the isotopic distributions produced in the reactions with the two projectiles largely differing in the initial neutron-to-proton ratio N/Z (^{124}Xe with $N/Z = 1.30$ and ^{136}Xe with $N/Z = 1.52$). A slightly enhanced production of more neutron-rich isotopes is observed in the isotopic distributions of the lightest elements ($Z \approx 5$–9) measured in the fragmentation of the more neutron-rich ^{136}Xe projectile. This enhancement of cross sections for neutron-rich isotopes is replaced by a shift of the isotopic distributions toward more neutron-rich isotopes for elements with charge above $Z \approx 10$. A clear difference between the positions of the maxima of the isotopic distributions from fragmentation of ^{124}Xe and

^{136}Xe projectiles may be observed, which increases with increasing nuclear charge. The largest difference is observed for elements in the vicinity of the projectile, since here a pronounced memory on the initial isotopic composition is preserved as a result of the rather low excitation energies acquired in the collision. With decreasing nuclear charge, this memory is considerably reduced because of the higher excitation energies introduced in the collision and, thus, a longer deexcitation process. Nevertheless, already from this comparison it is obvious that the memory on the initial N/Z is preserved in the whole nuclear-charge range despite the influence of the evaporation process.

Apart from the observation that a more neutron-rich projectile results in more neutron-rich final residues, the isotopic distributions from the ^{136}Xe projectile appear to be broader, which is especially pronounced for elements in the vicinity of the projectile. The isotopic distribution of primary fragments produced by the initial collision transforms into the distribution of final fragments through the emission of neutrons, protons, and complex clusters. Due to the higher neutron excess of the ^{136}Xe projectile, the evaporation from elements close to the projectile may be viewed as progressing close to a horizontal line of constant Z in the chart of the nuclides, populating thus a rather broad range of isotopes of the same element. On the contrary, in the case of the less neutron-rich projectile ^{124}Xe, the competition between
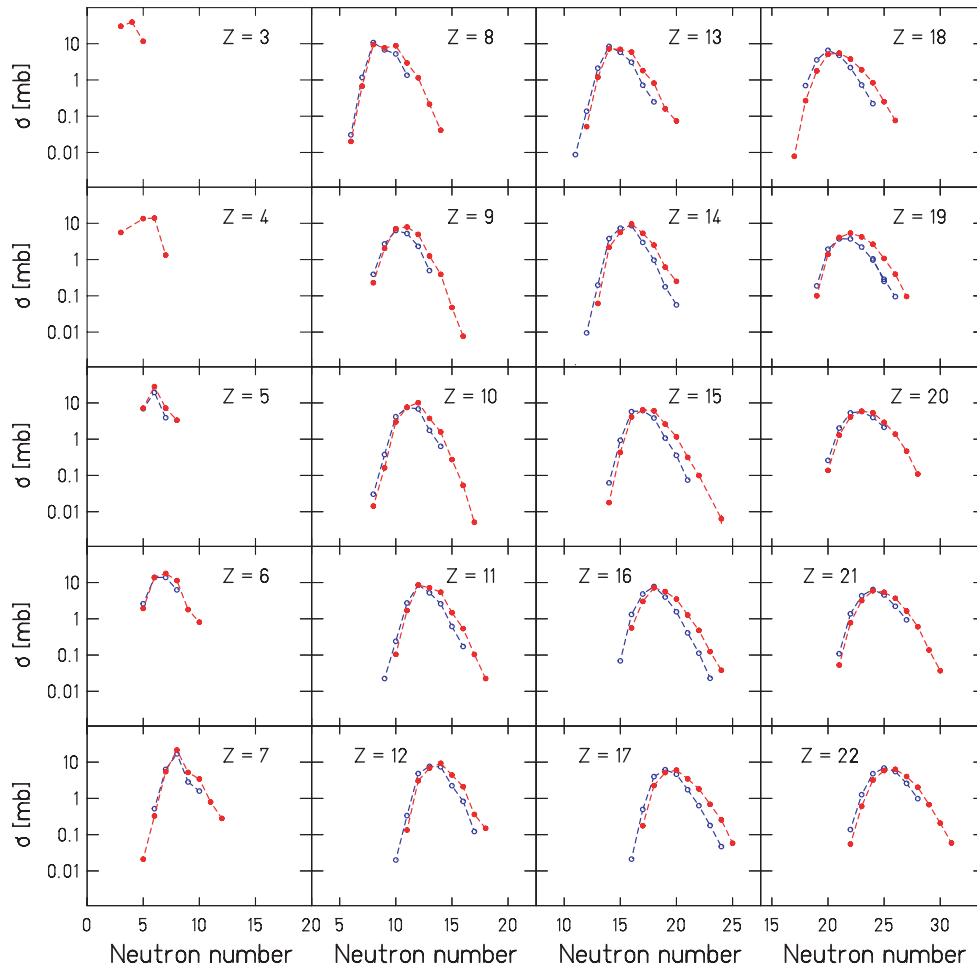
FIG. 7. (Color online) Angular-acceptance-integrated isotopic cross sections measured in ^{136}Xe + Pb (full red symbols) and ^{124}Xe + Pb (open blue symbols), for $Z = 3$–22. The dashed lines serve to guide the eye. Statistical error bars are smaller than the size of the symbols.

neutron and proton evaporation depopulates a given isotopic chain in favor of producing isotopes of lower elements. As a consequence, only a rather narrow range of isotopes of the same element is populated in the evaporation in the case of this less neutron-rich projectile. Narrower isotopic distributions in the vicinity of the projectile may, thus, be expected for ^{124}Xe.

In addition to the trends in the mean values and widths, another interesting feature may be observed in the final isotopic distributions from both experiments. In the nuclear-charge range $Z \approx 5$–15 a staggering in the cross sections of neighboring isotopes can be seen. This staggering is a manifestation of an even-odd effect resulting from the condensation process of heated nuclear matter while cooling down in the evaporation process [28]. As such, it can be considered as the manifestation of the passage from the normal liquid phase of the nucleus to its superfluid phase. The even-odd staggering disappears around $Z \sim 15$ because of the increasing competition of the γ emission as a consequence of an increasing level density below the particle emission threshold. In Ref. [28], a quantitative discussion of even-odd staggering in the production cross sections is given. It is remarkable in the present data that also for heavy nuclides in the vicinity of the projectile, an

even-odd staggering in the production cross sections is present ($Z = 53$). This is a new observation absent in the previous FRS experiments with heavier projectiles (Pb + Cu, Pb+^{1,2}H, Au+^{1}H) [20,29–31].

In both experiments, the charge-pickup reactions were also measured (isotopes with $Z > Z_{\text{projectile}}$). While for the less neutron-rich projectile, only single charge-pickup channels are observed ($Z = 55$), for ^{136}Xe, double charge-pickup residues were also detected ($Z = 56$). Charge-pickup reactions proceed [32,33] either through a quasielastic collision between a proton and a neutron of the target and the projectile nucleus, respectively, where the proton replaces the neutron inside the projectile-like fragment, or through the excitation of a projectile or a target nucleon into the $\Delta 1232$-resonance state and its subsequent decay. For the more neutron-rich projectile, the primary projectile-like fragment after the charge-pickup reaction is still rather neutron-rich, so neutron emission dominates in the evaporation process. As a consequence, the isotopes of the same nuclear charge as the excited projectile-like fragment are predominantly produced. Again, the competition between neutron and proton emission in the case of the primary projectile-like fragment from the less neutron-rich ^{124}Xe may be the reason why the double
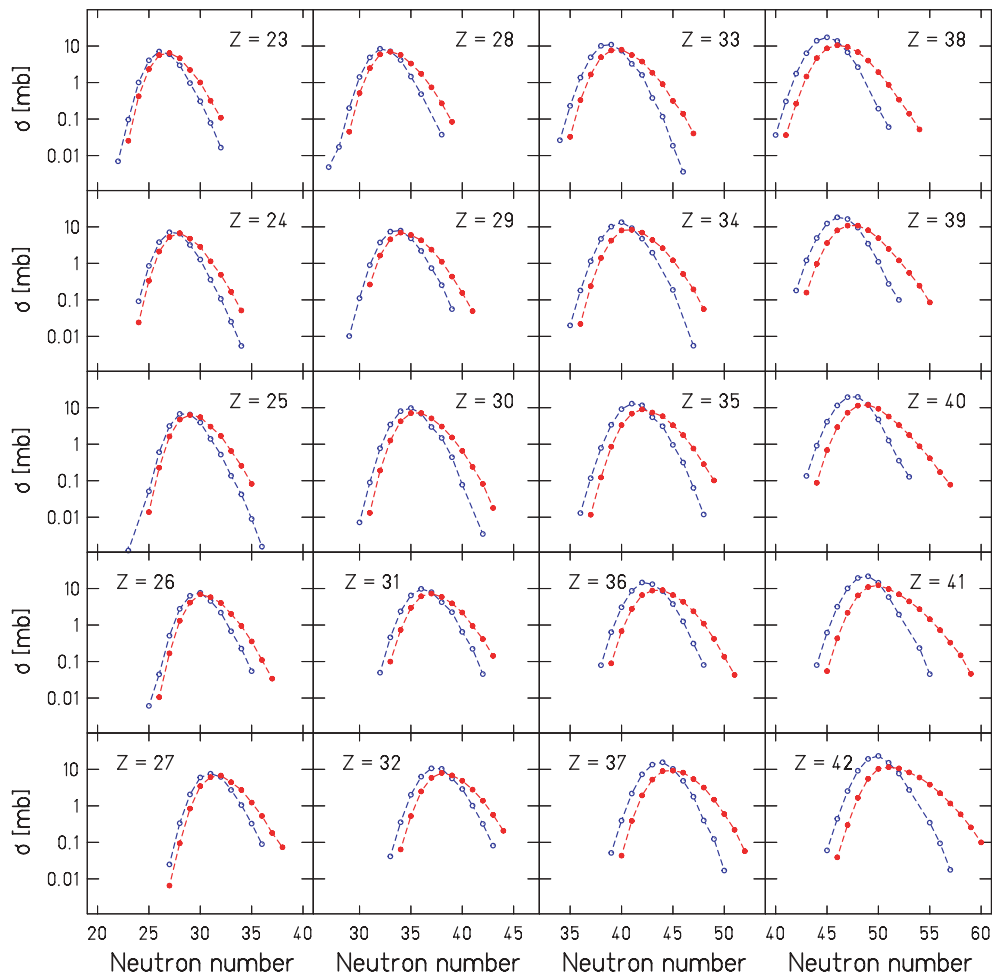
FIG. 8. (Color online) Same as Fig. 7, but for $Z = 23$–42.

charge-pickup residues (isotopes of the $Z = 56$ element) are not observed in the case of this projectile.

C. Mass and nuclear-charge distributions

To obtain the full production cross sections, the correction for the limited angular transmission of single isotopes through the FRS must be applied. This correction was performed only for isotopes of elements with $Z \geqslant 10$ in both experiments. The velocity distributions for the lighter elements reveal structures presumably originating from the overlap of contributions from different reaction mechanisms, which makes the determination of the transmission correction for these isotopes rather difficult. Therefore, the production cross sections in the following are restricted to the final residues in the nuclear-charge range $Z \geqslant 10$, where the transmission correction was evaluated under the assumption of isotropic Gaussian-shaped momentum distributions around the mean value of the emitting-source momentum.

The mass and nuclear-charge distributions determined from the production cross sections measured in both experiments and corrected for the FRS angular transmission are presented in Fig. 10. Systematic uncertainties are the same as those

of the nuclide yields in the corresponding element and mass range, respectively. The slight depletion observed in the mass distribution for the reaction ^{124}Xe + Pb in the mass range $A \sim 40$ is a consequence of the fact that the isotopes of the element $Z = 19$ could not be reconstructed from the light-fragment settings. Rather, they had to be extracted from the heavy-fragment settings where they passed the FRS rather close to its borders, and consequently the yields of these isotopes were slightly cut by the FRS acceptance. Similarly, a slightly lower value of the total elemental cross section of this element is observed in the charge distribution.

Overall, rather similar trends for both projectiles are seen, characterized by steeply decreasing cross sections of the heavy residues with decreasing mass and nuclear charge, followed by a plateau of rather constant cross sections below $A \sim 65$ ($Z \sim 30$) and an exponential increase of the cross sections of the light fragments. In the earlier investigations of the mass and nuclear-charge distributions, the shape of the nuclear charge or mass distributions was observed to evolve from two distinct regions corresponding to heavy residues close to the projectile (or target) and to light fragments produced in evaporation, toward the U-shape nuclear charge and mass distributions [34]. The former case is typical for the sequential evaporation from a
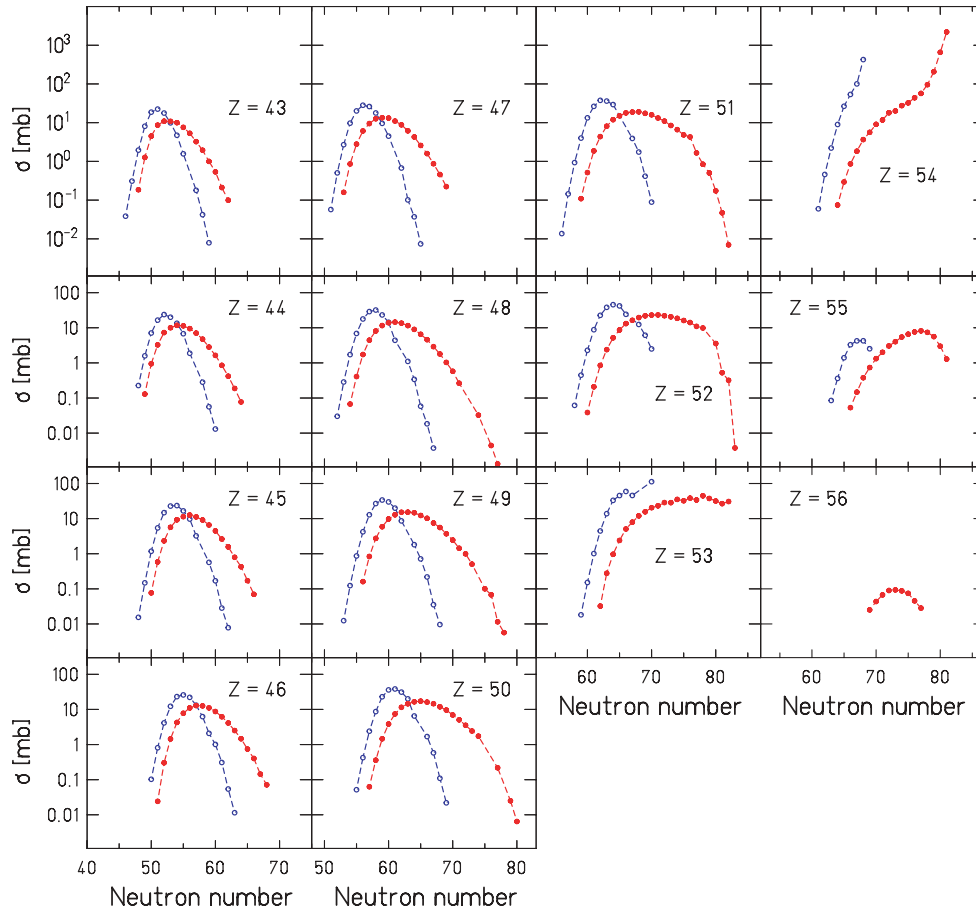
FIG. 9. (Color online) Same as Fig. 7, but for $Z = 43–56$.

moderately excited nuclear source, while the U-shape distributions were usually observed in collisions where considerably higher excitation energies were introduced, leading eventually to the simultaneous breakup of the highly excited nuclear source [35]. Exploring the mass or nuclear-charge distributions measured in the present experiments, it is observed that the cross sections of residues in the plateau regions are approximately only a factor of 2–3 lower than the cross sections of the lightest fragments observed. This moderate change of the cross section as a function of mass and nuclear charge is more similar to trends of the mass and nuclear-charge distributions measured in reactions with considerably high excitation energies introduced in the collision, which may proceed through a breakup stage.

D. Mean *N*-over-*Z* ratio

Already from the comparison of the measured isotopic distributions, the enhanced production of more neutron-rich isotopes in the ^{136}Xe + Pb reaction could be observed. This trend suggests a dependence of the final isotopic composition on the N/Z of the projectile and may be studied in more detail if the mean values of the isotopic distributions from both experiments are compared. For this purpose, the mean

N-over-Z ratio ($\langle N \rangle / Z$) is determined from each isotopic distribution allowing a direct comparison with the N/Z of the two projectiles. Figure 11 shows the $\langle N \rangle / Z$ of the final residues measured in both experiments as a function of the nuclear charge.

The data are compared with the stability line obtained from Ref. [36]. Three different regions may be identified in the data.

1. Vicinity of the projectile

For nuclei in the vicinity of the projectile (app. $50 \leqslant Z \leqslant 54$), a rather steep decrease of the $\langle N \rangle / Z$ values is observed with decreasing nuclear charge for the ^{136}Xe projectile. This decrease appears to be less steep for the ^{124}Xe projectile. These observations may be understood as a consequence of very peripheral collisions producing the final residues in the vicinity of the projectile, where rather low excitation energies are introduced. For the ^{136}Xe projectile, neutron emission dominates the evaporation process for the primary fragments in this nuclear-charge range. This prevalent neutron emission strongly affects the N/Z of the residues, which results in the steep trend observed in the figure. On the contrary, in the case of the less neutron-rich projectile ^{124}Xe, the emission of neutrons and protons may compete in
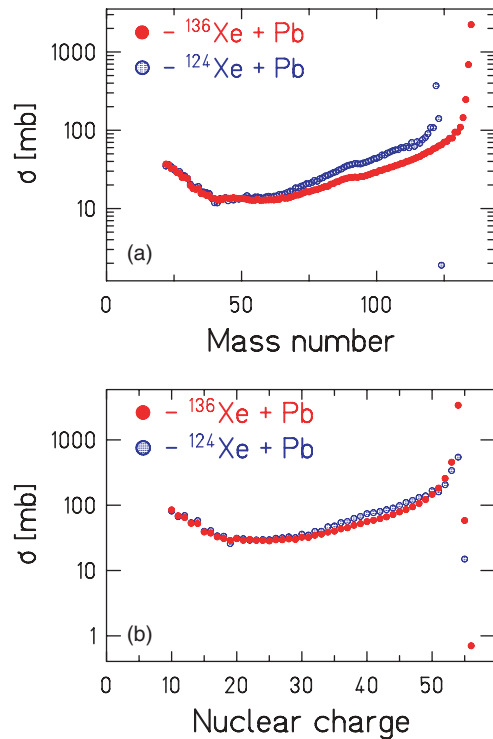
FIG. 10. (Color online) Mass and nuclear-charge distributions measured in the ^{136}Xe + Pb and ^{124}Xe + Pb experiments. Statistical error bars are smaller than the size of the symbols.

the evaporation process already at rather low initial excitation energies, which makes the change of the N/Z of residues close to this projectile less steep.
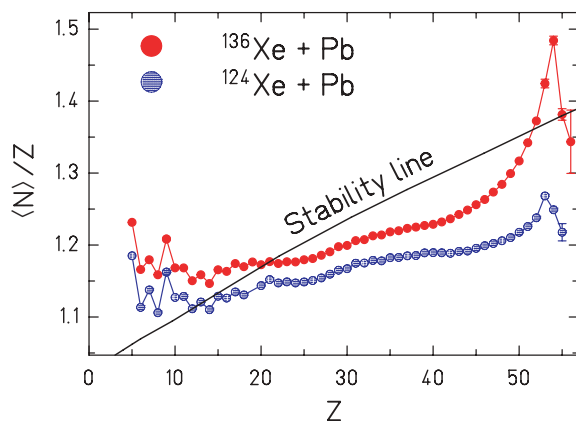
FIG. 11. (Color online) Comparison of the $\langle N \rangle/Z$ of final residues determined from the isotopic distributions of the reactions ^{136}Xe$(N/Z = 1.52)$ + Pb and ^{124}Xe$(N/Z = 1.30)$ + Pb at $1A$ GeV. Values for $Z < 10$ are derived from angular-acceptance-integrated cross sections. The full line represents the $\langle N \rangle/Z$ of the stable isotopes [36]. Statistical error bars are not shown when they are smaller than the size of the symbols. Systematic uncertainties are negligible.

2. Below $Z \approx 50$

In the region below $Z \approx 50$, the transition to a smoother dependence of $\langle N \rangle/Z$ on the nuclear charge occurs. This is a consequence of higher excitation energies introduced in the collision and, thus, the competing emission of neutrons, protons, and eventually more complex clusters during the evaporation. Nevertheless, despite the decreasing nuclear charge (i.e., increasing excitation energy acquired in the collision), the final residues from the ^{136}Xe projectile remain to be more neutron-rich on average than the residues from ^{124}Xe in the whole nuclear-charge range. This was already observed in the relative shift of the isotopic distributions from the two projectiles. This observation is particularly interesting, since as discussed in Refs. [37,38], the isotopic composition of the final residues after a long evaporation process is expected to gradually approach the region of equilibrium neutron- and proton-emission probabilities, known as the evaporation-attractor line (EAL) or the residue corridor [37,38]. Thus, the isotopic composition of the final residues far from the projectile should no longer depend on the N/Z of the initial system. The extent to which the corridor appears to be "attractive" to the final residues depends, however, on the neutron or proton excess of the initial system, which may, due to the emission of more complex clusters in the evaporation, even prevent the final residues from reaching the residue corridor at all [38]. At the same time, the highly excited nuclear source can undergo a simultaneous breakup process, which may affect the isotopic composition as well as the excitation energy of the produced fragments that enter into the evaporation process. As a consequence, the final residues may be prevented from ever reaching the residue corridor [9]. The difference in the final $\langle N \rangle/Z$ of the final residues is an interesting observation, which may be used to investigate the relative importance of different reaction mechanisms leading to the final isotopic composition. This will be the subject of a forthcoming paper.

3. Below $Z \approx 15$

The $\langle N \rangle/Z$ of the lightest nuclei (below $Z \approx 15$) strongly staggers as a function of Z. This nuclear-charge range coincides with the region where the even-odd effect is particularly pronounced in the isotopic distributions, as discussed earlier. It is the enhancement of the production of the even-N stable isotopes (mostly $N = Z$) for even nuclear charge, which is responsible for the shift of the mean values of the even-Z isotopic distributions toward the less neutron-rich isotopes. This shift is reflected in the lower values of the $\langle N \rangle/Z$ of the final residues with even nuclear charge.

Overall, the $\langle N \rangle/Z$ provides rich experimental information, which upon comparison with nuclear-reaction codes, can help to extract additional information on the properties of highly excited nuclear systems [9].

V. SUMMARY

Within the current paper, the velocity distributions and cross sections of residues produced in the interactions of ^{124}Xe $(N/Z = 1.30)$ and ^{136}Xe $(N/Z = 1.52)$ projectiles with a lead

target were investigated. Both experiments were performed at a high-resolution magnetic spectrometer, the fragment separator of GSI, which allows the identification of reaction residues in the complete mass and nuclear-charge range. More than 1100 nuclides were measured in both experiments, covering the isotopes of $Z = 3$–56 elements in the ^{136}Xe + Pb reaction and $Z = 5$–55 elements in the ^{124}Xe + Pb system.

The angular-acceptance-integrated cross sections were determined for all isotopes in this nuclear-charge range. The transmission-corrected production cross sections, which correspond to the full production of single isotopes, were determined for isotopes in the nuclear-charge range $Z = 10$–55(56) for the ^{124}Xe and ^{136}Xe projectile, respectively. The production cross sections measured in each experiment range over several orders of magnitude from 1 μb to 2b with a relative uncertainty corresponding to 8–15% in most cases. The longitudinal momenta of the residues were measured with a relative uncertainty of 5×10^{-4}, which allows one to investigate the mechanisms responsible for fragment formations.

The measured isotopic distributions reveal an enhancement of cross sections for neutron-rich isotopes of the lightest elements produced in the reaction ^{136}Xe + Pb as compared to the reaction ^{124}Xe + Pb. This is then gradually replaced by a shift of the mean values of the isotopic distributions in the reaction ^{136}Xe + Pb toward the more neutron-rich side for elements with nuclear charge above $Z \approx 10$. This observation reveals a clear memory on the N/Z of the projectile being preserved over the whole nuclear-charge range despite the influence of the evaporation process, and thus the isotopic distributions may be used to investigate the relative importance of different reaction mechanisms leading to the final isotopic composition. Furthermore, these data are of importance for studying the isospin effect in the symmetry energy and for studying the effect of evaporation on the observables related to the equation of state.

APPENDIX: COMPILATION OF THE CROSS SECTIONS MEASURED IN THE ^{136}Xe + Pb AND ^{124}Xe + Pb REACTIONS

The transmission-corrected production cross sections measured in the two experiments, which were analyzed within this work, are listed in Table I. The corresponding absolute uncertainties, which include both statistical and systematic uncertainties, are indicated.

TABLE I. Production cross sections of isotopes of $Z = 10$–55(56) elements measured in the ^{136}Xe + Pb and ^{124}Xe + Pb experiments. The absolute errors include both statistical and systematic uncertainties.

^{136}Xe + Pb, $1A$ GeV				^{124}Xe + Pb, $1A$ GeV			
Z	N	σ[mb]	$\Delta\sigma$[mb]	Z	N	σ[mb]	$\Delta\sigma$[mb]
10	8	0.060	0.008	10	8	0.146	0.015
10	9	0.630	0.073	10	9	1.68	0.17
10	10	10.7	1.2	10	10	17.3	1.7
10	11	25.6	2.9	10	11	29.1	2.9
10	12	31.7	3.6	10	12	25.0	2.5
10	13	10.9	1.2	10	13	6.04	0.60
10	14	4.33	0.49	10	14	2.07	0.21
10	15	0.706	0.083				
10	16	0.130	0.016	11	9	0.092	0.010
10	17	0.012	0.002	11	10	0.921	0.092
				11	11	9.87	0.98
11	10	0.349	0.040	11	12	29.3	2.9
11	11	5.27	0.59	11	13	16.7	1.7
11	12	24.7	2.8	11	14	7.90	0.79
11	13	19.7	2.2	11	15	1.79	0.18
11	14	13.9	1.6	11	16	0.477	0.048
11	15	3.59	0.40				
11	16	1.24	0.14	12	10	0.071	0.008
11	17	0.227	0.027	12	11	1.122	0.112
11	18	0.047	0.007	12	12	15.4	1.5

TABLE I. *(Continued.)*

Z	N	σ [mb]	$\Delta\sigma$ [mb]	Z	N	σ [mb]	$\Delta\sigma$ [mb]
		^{136}Xe + Pb, 1A GeV				^{124}Xe + Pb, 1A GeV	
12	11	0.390	0.044	12	13	23.0	2.2
12	12	8.38	0.93	12	14	21.3	2.1
12	13	17.5	1.9	12	15	6.12	0.61
12	14	22.6	2.5	12	16	2.17	0.22
12	15	10.2	1.1	12	17	0.307	0.031
12	16	4.61	0.51				
12	17	0.752	0.085	13	11	0.027	0.003
12	18	0.298	0.035	13	12	0.407	0.041
				13	13	5.98	0.59
13	12	0.133	0.016	13	14	22.6	2.3
13	13	2.90	0.31	13	15	15.0	1.5
13	14	16.6	1.8	13	16	7.63	0.76
13	15	15.3	1.6	13	17	1.71	0.17
13	16	12.3	1.3	13	18	0.569	0.057
13	17	3.62	0.39				
13	18	1.56	0.17	14	12	0.027	0.003
13	19	0.294	0.035	14	13	0.529	0.053
13	20	0.131	0.018	14	14	9.73	0.97
				14	15	18.1	1.8
14	13	0.143	0.016	14	16	20.4	2.0
14	14	4.81	0.50	14	17	6.77	0.67
14	15	11.8	1.2	14	18	2.11	0.21
14	16	19.3	2.0	14	19	0.377	0.038
14	17	10.2	1.1	14	20	0.116	0.012
14	18	4.64	0.49				
14	19	1.10	0.12	15	14	0.152	0.016
14	20	0.432	0.048	15	15	2.19	0.22
				15	16	13.0	1.3
15	14	0.038	0.005	15	17	13.4	1.3
15	15	0.875	0.089	15	18	8.12	0.81
15	16	7.97	0.81	15	19	2.19	0.22
15	17	12.0	1.2	15	20	0.710	0.071
15	18	10.9	1.1	15	21	0.144	0.015
15	19	4.51	0.46				
15	20	1.96	0.20	16	15	0.156	0.016
15	21	0.513	0.054	16	16	2.87	0.29
15	22	0.158	0.018	16	17	10.2	1.0
15	23	–	–	16	18	15.8	1.6
15	24	0.010	0.003	16	19	7.88	0.78
				16	20	3.00	0.30
16	16	1.06	0.16	16	21	0.765	0.076
16	17	5.50	0.81	16	22	0.205	0.021
16	18	12.7	1.9	16	23	0.041	0.004
16	19	9.62	1.43				
16	20	5.78	0.86	17	16	0.044	0.005
16	21	2.04	0.30	17	17	1.00	0.10
16	22	0.753	0.113	17	18	7.84	0.78
16	23	0.190	0.029	17	19	11.8	1.2
16	24	0.057	0.010	17	20	8.62	0.86
				17	21	3.15	0.31
17	17	0.317	0.052	17	22	1.12	0.11
17	18	3.94	0.64	17	23	0.309	0.031
17	19	8.71	1.41	17	24	0.079	0.008
17	20	9.85	1.60				
17	21	5.54	0.90	18	18	1.33	0.15
17	22	2.85	0.46	18	19	6.60	0.74

TABLE I. *(Continued.)*

	^{136}Xe + Pb, 1A GeV				^{124}Xe + Pb, 1A GeV		
Z	N	σ[mb]	$\Delta\sigma$[mb]	Z	N	σ[mb]	$\Delta\sigma$[mb]
17	23	1.04	0.17	18	20	11.8	1.3
17	24	0.381	0.063	18	21	8.39	0.93
17	25	0.084	0.015	18	22	3.78	0.42
				18	23	1.22	0.13
18	17	0.014	0.002	18	24	0.366	0.041
18	18	0.456	0.057				
18	19	2.93	0.37	19	19	0.388	0.055
18	20	8.27	1.03	19	20	3.88	0.55
18	21	8.71	1.09	19	21	7.32	1.03
18	22	5.85	0.73	19	22	7.12	1.01
18	23	2.89	0.36	19	23	4.14	0.58
18	24	1.24	0.16	19	24	1.77	0.25
18	25	0.366	0.047	19	25	0.512	0.072
18	26	0.109	0.018	19	26	0.167	0.024
				20	20	0.444	0.050
19	19	0.161	0.019	20	21	3.39	0.38
19	20	2.19	0.25	20	22	8.68	0.97
19	21	6.26	0.72	20	23	9.26	1.03
19	22	8.07	0.93	20	24	6.24	0.69
19	23	6.25	0.72	20	25	3.27	0.37
19	24	3.84	0.44				
19	25	1.52	0.17	21	21	0.179	0.021
19	26	0.549	0.064	21	22	2.20	0.25
19	27	0.131	0.018	21	23	6.80	0.76
				21	24	9.93	1.11
20	20	0.209	0.019	21	25	6.91	0.77
20	21	1.92	0.17	21	26	3.30	0.37
20	22	5.97	0.54	21	27	1.38	0.15
20	23	8.46	0.77				
20	24	7.51	0.68	22	22	0.22	0.02
20	25	4.03	0.37	22	23	1.98	0.22
20	26	1.86	0.17	22	24	7.36	0.82
20	27	0.620	0.057	22	25	10.4	1.15
20	28	0.144	0.014	22	26	8.15	0.91
				22	27	3.79	0.42
21	21	0.077	0.007	22	28	1.42	0.16
21	22	1.11	0.09				
21	23	4.44	0.39	23	22	0.011	0.001
21	24	8.16	0.73	23	23	0.150	0.015
21	25	7.27	0.65	23	24	1.53	0.15
21	26	4.87	0.43	23	25	6.08	0.61
21	27	2.14	0.19	23	26	10.4	1.0
21	28	0.777	0.069	23	27	8.63	0.86
21	29	0.174	0.017	23	28	4.25	0.42
21	30	0.046	0.006	23	29	1.36	0.14
				23	30	0.426	0.043
22	22	0.076	0.007	23	31	0.107	0.011
22	23	0.825	0.073	23	32	0.022	0.002
22	24	4.27	0.37				
22	25	7.72	0.67	24	24	0.140	0.014
22	26	8.23	0.72	24	25	1.28	0.13
22	27	5.14	0.45	24	26	5.65	0.56
22	28	2.55	0.22	24	27	10.4	1.0
22	29	0.835	0.074	24	28	9.40	0.94

TABLE I. *(Continued.)*

^{136}Xe + Pb, 1A GeV				^{124}Xe + Pb, 1A GeV			
Z	N	σ [mb]	$\Delta\sigma$ [mb]	Z	N	σ [mb]	$\Delta\sigma$ [mb]
22	30	0.254	0.023	24	29	4.52	0.45
22	31	0.071	0.010	24	30	1.78	0.18
				24	31	0.493	0.049
23	23	0.034	0.003	24	32	0.145	0.015
23	24	0.549	0.048	24	33	0.034	0.004
23	25	3.00	0.26	24	34	0.007	0.001
23	26	7.16	0.61				
23	27	8.09	0.69	25	23	0.002	0.0006
23	28	5.70	0.49	25	24	–	–
23	29	2.69	0.23	25	25	0.077	0.0079
23	30	1.21	0.10	25	26	0.895	0.089
23	31	0.379	0.033	25	27	4.59	0.46
23	32	0.128	0.012	25	28	9.73	0.97
24	24	0.031	0.003	25	29	9.24	0.92
24	25	0.423	0.036	25	30	5.51	0.55
24	26	2.64	0.22	25	31	1.93	0.19
24	27	6.46	0.54	25	32	0.711	0.071
24	28	8.17	0.69	25	33	0.185	0.019
24	29	5.70	0.48	25	34	0.057	0.006
24	30	3.37	0.29	25	35	0.012	0.001
24	31	1.33	0.11	25	36	0.0021	0.0003
24	32	0.565	0.048				
24	33	0.190	0.017	26	25	0.008	0.002
24	34	0.058	0.008	26	26	0.059	0.009
				26	27	0.661	0.103
25	25	0.017	0.002	26	28	3.55	0.55
25	26	0.278	0.024	26	29	7.99	1.25
25	27	1.97	0.16	26	30	9.53	1.49
25	28	5.67	0.47	26	31	5.61	0.88
25	29	7.45	0.62	26	32	2.67	0.42
25	30	6.44	0.53	26	33	0.813	0.127
25	31	3.50	0.29	26	34	0.269	0.042
25	32	1.93	0.16	26	35	0.064	0.010
25	33	0.735	0.062				
25	34	0.287	0.024	27	27	0.031	0.005
25	35	0.091	0.009	27	28	0.417	0.060
				27	29	2.53	0.37
26	26	0.013	0.002	27	30	7.31	1.05
26	27	0.199	0.017	27	31	9.15	1.32
26	28	1.55	0.13	27	32	7.38	1.07
26	29	4.80	0.39	27	33	3.22	0.47
26	30	8.01	0.65	27	34	1.23	0.18
26	31	6.57	0.53	27	35	0.378	0.055
26	32	4.56	0.37	27	36	0.103	0.015
26	33	2.26	0.18				
26	34	1.05	0.09	28	27	0.006	0.001
26	35	0.390	0.032	28	28	0.021	0.003
26	36	0.119	0.011	28	29	0.240	0.032
26	37	0.037	0.004	28	30	1.69	0.22
				28	31	5.75	0.76
27	27	0.008	0.001	28	32	9.83	1.31
27	28	0.110	0.009	28	33	8.27	1.10
27	29	0.97	0.08	28	34	4.75	0.63
27	30	3.95	0.31	28	35	1.66	0.22
27	31	6.88	0.55	28	36	0.544	0.072

TABLE I. *(Continued.)*

^{136}Xe + Pb, 1A GeV				^{124}Xe + Pb, 1A GeV			
Z	N	σ[mb]	$\Delta\sigma$[mb]	Z	N	σ[mb]	$\Delta\sigma$[mb]
27	32	7.56	0.60	28	37	–	–
27	33	4.92	0.39	28	38	0.042	0.006
27	34	2.99	0.24				
27	35	1.34	0.11	29	29	0.012	0.002
27	36	0.572	0.046	29	30	0.130	0.015
27	37	0.194	0.016	29	31	1.04	0.12
27	38	0.078	0.009	29	32	4.31	0.51
				29	33	8.44	0.98
28	29	0.051	0.005	29	34	8.94	1.04
28	30	0.577	0.046	29	35	5.45	0.63
28	31	2.76	0.22	29	36	2.44	0.28
28	32	6.54	0.51	29	37	0.819	0.096
28	33	7.69	0.60	29	38	0.279	0.033
28	34	6.25	0.49	29	39	0.061	0.007
28	35	3.58	0.28				
28	36	1.87	0.15	30	30	0.008	0.002
28	37	0.786	0.062	30	31	0.098	0.011
28	38	0.284	0.023	30	32	0.836	0.091
28	39	0.088	0.008	30	33	3.80	0.41
				30	34	8.73	0.95
29	31	0.291	0.023	30	35	10.5	1.1
29	32	1.79	0.14	30	36	7.26	0.79
29	33	4.96	0.39	30	37	3.60	0.39
29	34	7.54	0.59	30	38	1.54	0.17
29	35	6.44	0.50	30	39	0.448	0.015
29	36	4.56	0.36	30	40	0.104	0.012
29	37	2.52	0.20	30	41	0.020	0.002
29	38	1.17	0.09	30	42	0.0034	0.0005
29	39	0.455	0.036				
29	40	0.162	0.013	31	32	0.055	0.006
29	41	0.051	0.005	31	33	0.489	0.048
				31	34	2.55	0.25
30	31	0.014	0.002	31	35	6.95	0.68
30	32	0.207	0.017	31	36	10.3	1.0
30	33	1.36	0.11	31	37	8.33	0.82
30	34	4.54	0.35	31	38	4.32	0.42
30	35	7.55	0.59	31	39	2.29	0.23
30	36	7.56	0.59	31	40	0.861	0.088
30	37	5.34	0.42	31	41	0.272	0.028
30	38	3.19	0.25	31	42	0.041	0.004
30	39	1.59	0.12				
30	40	0.681	0.054	32	33	0.044	0.004
30	41	0.248	0.020	32	34	0.371	0.036
30	42	0.084	0.008	32	35	2.12	0.20
30	43	0.018	0.003	32	36	6.61	0.63
				32	37	11.1	1.1
31	33	0.107	0.008	32	38	10.7	1.0
31	34	0.782	0.058	32	39	5.86	0.56
31	35	3.14	0.23	32	40	2.99	0.29
31	36	6.43	0.47	32	41	1.06	0.10
31	37	7.61	0.56	32	42	0.331	0.034
31	38	6.13	0.45	32	43	0.084	0.008
31	39	4.06	0.30				
31	40	2.27	0.17	33	34	0.035	0.003
31	41	0.974	0.072	33	35	0.240	0.017

TABLE I. *(Continued.)*

Z	N	σ [mb]	Δσ [mb]	Z	N	σ [mb]	Δσ [mb]
	^{136}Xe + Pb, 1A GeV				^{124}Xe + Pb, 1A GeV		
31	42	0.422	0.031	33	36	1.41	0.10
31	43	0.146	0.012	33	37	5.08	0.36
				33	38	10.4	0.7
32	34	0.068	0.006	33	39	11.1	0.8
32	35	0.552	0.041	33	40	7.54	0.54
32	36	2.60	0.19	33	41	3.49	0.25
32	37	6.12	0.44	33	42	1.54	0.11
32	38	8.26	0.60	33	43	0.389	0.031
32	39	7.04	0.51	33	44	0.159	0.013
32	40	5.02	0.36	33	45	0.018	0.002
32	41	2.85	0.21	33	46	0.0035	0.0004
32	42	1.41	0.10				
32	43	0.58	0.04	34	35	0.022	0.002
32	44	0.211	0.016	34	36	0.184	0.013
				34	37	1.18	0.08
33	35	0.0341	0.0030	34	38	4.81	0.34
33	36	0.342	0.025	34	39	10.3	0.7
33	37	1.72	0.12	34	40	13.6	0.9
33	38	5.10	0.37	34	41	9.33	0.66
33	39	7.79	0.56	34	42	5.04	0.36
33	40	8.15	0.59	34	43	1.98	0.15
33	41	5.79	0.42	34	44	–	–
33	42	3.83	0.28	34	45	0.231	0.019
33	43	1.89	0.14	34	46	–	–
33	44	0.914	0.066	34	47	0.0056	0.0005
33	45	0.318	0.023				
33	46	0.140	0.016	35	36	0.013	0.001
33	47	0.041	0.004	35	37	0.119	0.009
				35	38	0.798	0.057
34	36	0.023	0.002	35	39	3.46	0.25
34	37	0.244	0.018	35	40	9.27	0.66
34	38	1.44	0.10	35	41	13.0	0.9
34	39	4.32	0.31	35	42	11.6	0.8
34	40	8.16	0.58	35	43	5.53	0.39
34	41	8.45	0.60	35	44	2.97	0.21
34	42	7.08	0.50	35	45	0.973	0.071
34	43	4.44	0.32	35	46	0.274	0.022
34	44	2.63	0.19	35	47	0.133	0.013
34	45	1.22	0.09	35	48	0.009	0.001
34	46	0.513	0.037				
34	47	0.195	0.015	36	38	0.079	0.006
34	48	0.056	0.005	36	39	0.639	0.045
				36	40	3.09	0.22
35	37	0.012	0.001	36	41	8.73	0.62
35	38	0.126	0.009	36	42	14.6	1.0
35	39	0.873	0.063	36	42	14.6	1.0
35	40	3.39	0.24	36	43	13.2	0.9
35	41	6.97	0.49	36	44	8.53	0.60
35	42	9.10	0.65	36	45	3.72	0.27
35	43	7.46	0.53	36	46	1.24	0.09
35	44	5.88	0.42	36	47	0.329	0.025
35	45	3.33	0.24	36	48	0.080	0.006
35	46	1.78	0.13				
35	47	0.766	0.055	37	39	0.047	0.004
35	48	0.285	0.021	37	40	0.393	0.028

TABLE I. *(Continued.)*

Z	N	σ[mb]	Δσ[mb]	Z	N	σ[mb]	Δσ[mb]
\multicolumn{4}{}{^{136}Xe + Pb, 1*A* GeV}	\multicolumn{4}{}{^{124}Xe + Pb, 1*A* GeV}			
35	49	0.102	0.009	37	41	2.18	0.15
				37	42	7.33	0.52
36	39	0.091	0.007	37	43	13.4	0.9
36	40	0.686	0.049	37	44	15.5	1.1
36	41	2.79	0.20	37	45	10.2	0.7
36	42	6.69	0.47	37	46	5.06	0.36
36	43	8.89	0.63	37	47	1.72	0.12
36	44	9.09	0.64	37	48	0.380	0.030
36	45	6.68	0.47	37	49	0.126	0.009
36	46	4.36	0.31	37	50	0.017	0.002
36	47	2.38	0.17				
36	48	1.09	0.08	38	40	0.034	0.003
36	49	0.419	0.030	38	41	0.296	0.021
36	50	0.136	0.010	38	42	1.74	0.12
36	51	0.043	0.007	38	43	6.37	0.45
				38	44	13.9	0.9
37	40	0.044	0.005	38	45	17.2	1.2
37	41	0.391	0.028	38	46	13.7	1.0
37	42	1.95	0.14	38	47	6.69	0.47
37	43	5.29	0.38	38	48	2.70	0.19
37	44	9.05	0.64	38	49	–	–
37	45	9.28	0.66	38	50	0.194	0.014
37	46	8.17	0.58	38	51	0.060	0.007
37	47	5.43	0.38				
37	48	3.18	0.23	39	42	0.178	0.013
37	49	1.48	0.11	39	43	1.20	0.09
37	50	0.595	0.043	39	44	4.93	0.35
37	51	0.222	0.016	39	45	12.3	0.9
37	52	0.057	0.005	39	46	18.2	1.3
				39	47	16.2	1.1
38	41	0.038	0.004	39	48	9.47	0.67
38	42	0.266	0.019	39	49	3.52	0.25
38	43	1.47	0.11	39	50	1.13	0.08
38	44	4.67	0.33	39	51	0.246	0.019
38	45	8.69	0.62	39	52	0.064	0.005
38	46	10.4	0.7				
38	47	9.51	0.67	40	43	0.132	0.009
38	48	6.86	0.49	40	44	0.899	0.064
38	49	4.00	0.28	40	45	4.13	0.29
38	50	1.92	0.14	40	46	11.5	0.8
38	51	0.867	0.062	40	47	19.4	1.4
38	52	0.340	0.025	40	48	19.6	1.4
38	53	0.140	0.011	40	49	12.0	0.9
38	54	0.052	0.006	40	50	4.75	0.34
				40	51	1.27	0.09
39	43	0.159	0.012	40	52	0.385	0.033
39	44	0.973	0.069	40	53	0.127	0.009
39	45	3.62	0.26				
39	46	8.04	0.57	41	44	0.078	0.006
39	47	10.9	0.8	41	45	0.615	0.044
39	48	10.9	0.8	41	46	3.16	0.22
39	49	8.09	0.57	41	47	10.0	0.7
39	50	4.89	0.35	41	48	19.3	1.4
39	51	2.50	0.18	41	49	21.5	1.5
39	52	1.21	0.09	41	50	14.2	1.0

TABLE I. *(Continued.)*

^{136}Xe + Pb, 1A GeV				^{124}Xe + Pb, 1A GeV			
Z	N	σ [mb]	$\Delta\sigma$ [mb]	Z	N	σ [mb]	$\Delta\sigma$ [mb]
39	53	0.551	0.039	41	51	5.78	0.41
39	54	0.245	0.018	41	52	1.99	0.14
39	55	0.085	0.007	41	53	–	–
				41	54	0.217	0.016
40	44	0.088	0.007	41	55	0.045	0.004
40	45	0.690	0.049				
40	46	2.93	0.21	42	45	0.055	0.004
40	47	7.31	0.52	42	46	0.438	0.031
40	48	11.4	0.8	42	47	2.53	0.18
40	49	11.9	0.8	42	48	9.13	0.65
40	50	9.39	0.66	42	49	19.3	1.4
40	51	5.72	0.41	42	50	23.2	1.6
40	52	3.34	0.24	42	51	14.9	1.1
40	53	1.78	0.13	42	52	7.61	0.54
40	54	0.874	0.062	42	53	2.71	0.19
40	55	0.411	0.030	42	54	–	–
40	56	0.172	0.013	42	55	0.346	0.026
40	57	0.078	0.007	42	56	0.093	0.007
				42	57	0.017	0.001
41	45	0.055	0.005				
41	46	0.433	0.032	43	46	0.035	0.003
41	47	2.18	0.16	43	47	0.308	0.022
41	48	6.47	0.46	43	48	1.94	0.14
41	49	11.0	0.8	43	49	8.05	0.57
41	50	12.2	0.9	43	50	18.7	1.3
41	51	9.69	0.69	43	51	22.3	1.6
41	52	6.96	0.49	43	52	17.6	1.2
41	53	4.44	0.31	43	53	9.78	0.69
41	54	2.71	0.19	43	54	4.60	0.33
41	55	1.44	0.10	43	55	1.39	0.10
41	56	0.724	0.052	43	56	–	–
41	57	0.329	0.024	43	57	0.186	0.014
41	58	0.148	0.012	43	58	0.042	0.003
41	59	0.046	0.006	43	59	0.008	0.001
42	46	0.039	0.005	44	48	0.221	0.016
42	47	0.298	0.022	44	49	1.56	0.11
42	48	1.66	0.12	44	50	7.06	0.50
42	49	5.54	0.39	44	51	16.5	1.2
42	50	10.4	0.7	44	52	23.6	1.7
42	51	11.4	0.8	44	53	19.8	1.4
42	52	10.6	0.8	44	54	13.3	0.9
42	53	8.24	0.58	44	55	6.58	0.5
42	54	5.97	0.42	44	56	1.67	0.13
42	55	3.82	0.27	44	57	–	–
42	56	2.22	0.16	44	58	0.340	0.025
42	57	1.16	0.08	44	59	0.087	0.007
42	58	0.585	0.042	44	60	0.013	0.001
42	59	0.257	0.019				
42	60	0.100	0.010	45	48	0.015	0.001
				45	49	0.142	0.010
43	48	0.186	0.014	45	50	1.16	0.08
43	49	1.27	0.09	45	51	5.42	0.38
43	50	4.51	0.32	45	52	14.7	1.0
43	51	8.64	0.61	45	53	22.6	1.6
43	52	10.9	0.8	45	54	23.4	1.7

TABLE I. *(Continued.)*

¹³⁶Xe + Pb, 1A GeV				¹²⁴Xe + Pb, 1A GeV			
Z	N	σ[mb]	Δσ[mb]	Z	N	σ[mb]	Δσ[mb]
43	53	10.8	0.77	45	55	16.3	1.2
43	54	9.99	0.71	45	56	9.60	0.68
43	55	7.57	0.54	45	57	4.62	0.34
43	56	5.32	0.38	45	58	–	–
43	57	3.24	0.23	45	59	0.582	0.042
43	58	1.94	0.14	45	60	0.169	0.012
43	59	0.999	0.071	45	61	0.028	0.002
43	60	0.538	0.039	45	62	0.0077	0.0007
43	61	0.211	0.016				
43	62	0.099	0.010	46	50	0.102	0.007
				46	51	0.804	0.057
44	49	0.129	0.010	46	52	4.11	0.29
44	50	0.946	0.068	46	53	12.2	0.9
44	51	3.26	0.23	46	54	23.1	1.6
44	52	7.29	0.52	46	55	25.8	1.8
44	53	10.0	0.7	46	56	21.6	1.5
44	54	11.7	0.8	46	57	13.1	0.9
44	55	11.4	0.8	46	58	6.20	0.44
44	56	9.46	0.67	46	59	1.97	0.14
44	57	7.05	0.50	46	60	0.805	0.087
44	58	4.72	0.33	46	61	0.315	0.023
44	59	2.82	0.20	46	62	0.086	0.007
44	60	1.63	0.12	46	63	0.011	0.001
44	61	0.852	0.061				
44	62	0.418	0.031	47	51	0.055	0.004
44	63	0.187	0.015	47	52	0.499	0.036
44	64	0.077	0.008	47	53	2.69	0.19
				47	54	9.70	0.69
45	50	0.077	0.006	47	55	20.1	1.4
45	51	0.584	0.042	47	56	28.2	2.0
45	52	2.33	0.17	47	57	25.7	1.8
45	53	5.65	0.40	47	58	17.8	1.3
45	54	9.24	0.65	47	59	9.20	0.65
45	55	11.4	0.8	47	60	3.92	0.28
45	56	12.6	0.9	47	61	–	–
45	57	11.2	0.8	47	62	0.566	0.040
45	58	9.17	0.65	47	63	0.169	0.013
45	59	6.57	0.47	47	64	0.036	0.003
45	60	4.47	0.32	47	65	0.0072	0.0006
45	61	2.63	0.19				
45	62	1.56	0.11	48	52	0.028	0.002
45	63	0.789	0.057	48	53	0.278	0.020
45	64	0.425	0.031	48	54	1.71	0.12
45	65	0.171	0.014	48	55	6.88	0.49
45	66	0.070	0.008	48	56	17.7	1.3
				48	57	28.7	2.0
46	51	0.024	0.003	48	58	31.5	2.2
46	52	0.303	0.022	48	59	22.9	1.63
46	53	1.45	0.10	48	60	14.1	1.0
46	54	4.27	0.30	48	61	6.34	0.45
46	55	7.78	0.55	48	62	–	–
46	56	11.1	0.8	48	63	1.09	0.08
46	57	12.9	0.9	48	64	0.274	0.020
46	58	12.7	0.9	48	65	0.058	0.004
46	59	11.1	0.8	48	66	0.018	0.002
46	60	8.73	0.62	48	67	0.0032	0.0005

TABLE I. *(Continued.)*

	^{136}Xe + Pb, $1A$ GeV				^{124}Xe + Pb, $1A$ GeV		
Z	N	σ [mb]	$\Delta\sigma$ [mb]	Z	N	σ [mb]	$\Delta\sigma$ [mb]
46	61	6.20	0.44	49	53	0.0124	0.0011
46	62	4.11	0.29	49	54	0.124	0.009
46	63	2.51	0.18	49	55	0.861	0.061
46	64	1.46	0.10	49	56	4.20	0.30
46	65	0.742	0.054	49	57	12.8	0.9
46	66	0.402	0.030	49	58	26.5	1.9
46	67	0.144	0.013	49	59	33.5	2.4
46	68	0.072	0.008	49	60	29.4	2.1
				49	61	19.7	1.4
47	53	0.159	0.012	49	62	9.55	0.68
47	54	0.859	0.062	49	63	–	–
47	55	2.79	0.20	49	64	1.54	0.11
47	56	6.11	0.43	49	65	0.729	0.052
47	57	9.49	0.67	49	66	0.218	0.016
47	58	12.6	0.9	49	67	0.033	0.003
47	59	13.4	0.9	49	68	0.0094	0.0008
47	60	13.1	0.9				
47	61	11.0	0.8	50	55	0.048	0.004
47	62	8.81	0.62	50	56	0.420	0.030
47	63	6.17	0.44	50	57	2.38	0.17
47	64	4.28	0.30	50	58	8.64	0.61
47	65	2.58	0.18	50	59	22.6	1.6
47	66	1.59	0.11	50	60	35.9	2.5
47	67	0.872	0.063	50	61	37.7	2.7
47	68	0.458	0.034	50	62	31.0	2.2
47	69	0.224	0.018	50	63	22.4	1.6
				50	64	6.51	0.46
48	54	0.067	0.006	50	65	–	–
48	55	0.408	0.030	50	66	1.66	0.12
48	56	1.73	0.12	50	67	0.581	0.042
48	57	4.43	0.31	50	68	0.108	0.008
48	58	8.09	0.57	50	69	0.022	0.002
48	59	11.6	0.8				
48	60	13.9	1.0	51	56	0.014	0.001
48	61	14.5	1.0	51	57	0.144	0.010
48	62	13.5	1.0	51	58	0.927	0.066
48	63	11.5	0.9	51	59	3.95	0.28
48	64	8.99	0.64	51	60	13.3	0.9
48	65	6.51	0.46	51	61	26.7	1.9
48	66	4.58	0.32	51	62	36.9	2.6
48	67	2.90	0.21	51	63	36.1	2.6
48	68	1.79	0.13	51	64	28.6	2.0
48	69	1.03	0.07	51	65	–	–
48	70	0.576	0.043	51	66	–	–
48	71	0.263	0.022	51	67	3.88	0.27
48	72	–	–	51	68	1.73	0.12
48	73	–	–	51	69	0.417	0.030
48	74	0.033	0.004	51	70	0.087	0.006
48	75	–	–				
48	76	0.0044	0.0004	52	58	0.059	0.005
48	77	0.0013	0.0002	52	59	0.438	0.032
				52	60	2.26	0.16
49	56	0.161	0.012	52	61	8.74	0.62
49	57	0.834	0.060	52	62	22.5	1.6
49	58	2.73	0.19	52	63	36.7	2.6

TABLE I. *(Continued.)*

Z	N	σ[mb]	$\Delta\sigma$[mb]	Z	N	σ[mb]	$\Delta\sigma$[mb]
		^{136}Xe + Pb, 1A GeV				^{124}Xe + Pb, 1A GeV	
49	59	5.87	0.42	52	64	45.2	3.2
49	60	9.75	0.69	52	65	41.6	2.9
49	61	12.9	0.9	52	66	24.2	1.7
49	62	15.1	1.1	52	67	–	–
49	63	15.2	1.1	52	68	12.4	0.9
49	64	14.7	1.0	52	69	6.08	0.43
49	65	12.3	0.9	52	70	2.23	0.16
49	66	10.2	0.7				
49	67	7.50	0.53	53	59	0.018	0.002
49	68	5.57	0.39	53	60	0.145	0.011
49	69	3.70	0.26	53	61	0.973	0.070
49	70	2.44	0.17	53	62	4.41	0.31
49	71	1.43	0.10	53	63	13.8	1.0
49	72	0.993	0.080	53	64	31.0	2.2
49	73	0.505	0.051	53	65	45.3	3.2
49	74	–	–	53	66	59.0	4.2
49	75	0.101	0.017	53	67	40.7	2.9
49	76	0.068	0.006	53	68	–	–
49	77	0.012	0.001	53	69	–	–
49	78	0.0057	0.0005	53	70	112	8
				54	61	0.057	0.009
50	57	0.063	0.007	54	62	0.444	0.067
50	58	0.359	0.033	54	63	2.21	0.33
50	59	1.46	0.13	54	64	8.89	1.34
50	60	3.84	0.35	54	65	24.6	3.7
50	61	7.44	0.68	54	66	53.5	8.0
50	62	11.5	1.0	54	67	96.7	14.5
50	63	14.5	1.3	54	68	333	50
50	64	16.5	1.5				
50	66	16.2	1.5	55	63	0.076	0.013
50	67	14.6	1.3	55	64	0.360	0.062
50	68	11.9	1.1	55	65	1.34	0.23
50	69	9.58	0.87	55	66	3.52	0.60
50	70	6.96	0.63	55	67	4.22	0.72
50	71	5.07	0.46	55	68	3.75	0.64
50	72	3.54	0.32	55	69	1.70	0.29
50	73	2.43	0.22				
50	74	1.73	0.16				
50	75	–	–				
50	76	–	–				
50	77	0.218	0.021				
50	78	–	–				
50	79	0.025	0.002				
50	80	0.0064	0.0006				
51	59	0.109	0.011				
51	60	0.516	0.048				
51	61	1.87	0.17				
51	62	4.37	0.40				
51	63	8.10	0.73				
51	64	11.9	1.1				
51	65	15.1	1.4				
51	66	17.9	1.6				
51	67	18.8	1.7				
51	68	19.1	1.7				
51	69	17.4	1.6				

TABLE I. *(Continued.)*

^{136}Xe + Pb, $1A$ GeV				^{124}Xe + Pb, $1A$ GeV			
Z	N	σ[mb]	$\Delta\sigma$[mb]	Z	N	σ[mb]	$\Delta\sigma$[mb]
51	70	16.0	1.5				
51	71	13.2	1.2				
51	72	11.0	1.0				
51	73	8.46	0.77				
51	74	6.62	0.60				
51	75	4.84	0.44				
51	76	4.28	0.41				
51	77	1.66	0.17				
51	78	0.844	0.078				
51	79	0.502	0.049				
51	80	0.174	0.018				
51	81	0.047	0.004				
51	82	0.0070	0.0007				
52	60	0.039	0.006				
52	61	0.208	0.024				
52	62	0.849	0.095				
52	63	2.38	0.26				
52	64	5.18	0.57				
52	65	8.66	0.96				
52	66	13.1	1.5				
52	67	16.3	1.8				
52	68	19.5	2.2				
52	69	21.9	2.4				
52	70	22.9	2.5				
52	71	23.2	2.6				
52	72	22.0	2.4				
52	73	20.5	2.3				
52	74	18.5	2.0				
52	75	16.1	1.8				
52	76	14.1	1.6				
52	77	10.9	1.2				
52	78	9.86	1.11				
52	79	–	–				
52	80	3.56	0.39				
52	81	0.525	0.059				
52	82	0.319	0.035				
52	83	0.0038	0.0005				
53	62	0.032	0.005				
53	63	0.277	0.037				
53	64	0.966	0.127				
53	65	2.39	0.31				
53	66	5.07	0.66				
53	67	7.92	1.03				
53	68	11.9	1.6				
53	69	15.6	2.0				
53	70	20.5	2.7				
53	71	23.1	3.0				
53	72	28.7	3.7				
53	73	28.5	3.7				
53	74	35.2	4.6				
53	75	32.2	4.2				
53	76	38.3	5.0				
53	77	33.9	4.4				

TABLE I. *(Continued.)*

^{136}Xe + Pb, 1A GeV				^{124}Xe + Pb, 1A GeV			
Z	N	σ[mb]	$\Delta\sigma$[mb]	Z	N	σ[mb]	$\Delta\sigma$[mb]
53	78	44.5	5.8				
53	79	37.4	4.9				
53	80	31.7	4.3				
53	81	26.6	3.5				
53	82	30.6	3.9				
54	64	0.075	0.012				
54	65	0.294	0.045				
54	66	0.864	0.130				
54	67	1.83	0.28				
54	68	3.66	0.55				
54	69	5.63	0.85				
54	70	9.07	1.36				
54	71	11.7	1.8				
54	72	18.0	2.7				
54	73	20.1	3.0				
54	74	27.5	4.1				
54	75	32.5	4.9				
54	76	44.0	6.6				
54	77	57.0	8.6				
54	78	95.8	14.4				
54	79	207	31				
54	80	656	98				
54	81	2201	331				
55	66	0.053	0.010				
55	67	0.147	0.026				
55	68	0.377	0.065				
55	69	0.738	0.126				
55	70	1.32	0.23				
55	71	2.00	0.34				
55	72	3.04	0.52				
55	73	4.01	0.68				
55	74	5.45	0.93				
55	75	6.56	1.12				
55	76	7.60	1.29				
55	77	8.17	1.39				
55	78	7.39	1.26				
55	79	5.59	0.95				
55	80	2.98	0.51				
55	81	1.28	0.22				
56	69	0.025	0.005				
56	70	0.044	0.008				
56	71	0.067	0.012				
56	72	0.090	0.016				
56	73	0.093	0.016				
56	74	0.088	0.015				
56	75	0.075	0.013				
56	76	0.046	0.008				
56	77	0.028	0.005				

[1] M. B. Tsang, T. X. Liu, L. Shi, P. Danielewicz, C. K. Gelbke, X. D. Liu, W. G. Lynch, W. P. Tan, G. Verde, A. Wagner, H. S. Xu, W. A. Friedman, L. Beaulieu, B. Davin, R. T. de Souza, Y. Larochelle, T. Lefort, R. Yanez, V. E. Viola, Jr., R. J. Charity, and L. G. Sobotka, Phys. Rev. Lett. **92**, 062701 (2004).

[2] V. Baran, M. Colonna, M. Di Toro, M. Zielinska-Pfabé, and H. H. Wolter, Phys. Rev. C **72**, 064620 (2005).

[3] L. Tassan-Got and C. Stéphan, Nucl. Phys. **A524**, 121 (1991).

[4] B. Borderie, J. Phys. G: Nucl. Part. Phys. **28**, R217 (2002).

[5] J. Hüfner, K. Schäfer, and B. Schürmann, Phys. Rev. C **12**, 1888 (1975).

[6] W. Reisdorf and H. G. Ritter, Annu. Rev. Nucl. Part. Sci. **47**, 663 (1997).

[7] P. Senger, Prog. Part. Nucl. Phys. **53**, 1 (2004).

[8] G. A. Souliotis, D. V. Shetty, A. Keksis, E. Bell, M. Jandel, M. Veselsky, and S. J. Yennello, Phys. Rev. C **73**, 024606 (2006).

[9] K.-H. Schmidt, M. V. Ricciardi, A. Botvina, and T. Enqvist, Nucl. Phys. **A710**, 157 (2002).

[10] M. Colonna and M. B. Tsang, Eur. Phys. J. A **30**, 165 (2006).

[11] M. V. Ricciardi, T. Enqvist, J. Pereira, J. Benlliure, M. Bernas, E. Casarejos, V. Henzl, A. Kelić, J. Taïeb, and K.-H. Schmidt, Phys. Rev. Lett. **90**, 212302 (2003).

[12] L. Shi, P. Danielewicz, and R. Lacey, Phys. Rev. C **64**, 034601 (2001).

[13] H. Geissel, P. Armbruster, K. H. Behr, A. Brünle, K. Burkard, M. Chen, H. Folger, B. Franczak, H. Keller, O. Klepper, B. Langenbeck, F. Nickel, E. Pfeng, M. Pfützner, E. Roeckl, K. Rykaczewski, I. Schall, D. Schardt, C. Scheidenberger, K.-H. Schmidt, A. Schröter, T. Schwab, K. Sümmerer, M. Weber, G. Münzenberg, T. Brohm, H.-G. Clerc, M. Fauerbach, J.-J. Gaimard, A. Grewe, E. Hanelt, B. Knödler, M. Steiner, B. Voss, J. Weckenmann, C. Ziegler, A. Magel, H. Wollnik, J.-P. Dufour, Y. Fujita, D. J. Vieira, and B. Sherrill, Nucl. Instrum. Methods B **70**, 286 (1992).

[14] C. Ziegler, Diploma thesis, Institut für Kernphysik, TU Darmstadt (1992).

[15] A. Junghans, H.-G. Clerc, A. Grewe, M. de Jong, J. Müller, and K.-H. Schmidt, Nucl. Instrum. Methods A **370**, 312 (1996).

[16] B. Jurado, K.-H. Schmidt, and K.-H. Behr, Nucl. Instrum. Methods A **483**, 603 (2002).

[17] M. Pfützner, H. Geissel, G. Münzenberg, F. Nickel, C. Scheidenberger, K.-H. Schmidt, K. Sümmerer, T. Brohm, B. Voss, and H. Bichsel, Nucl. Instrum. Methods B **86**, 213 (1994).

[18] H. Stelzer, Nucl. Instrum. Methods A **310**, 103 (1991).

[19] J. Benlliure, J. Pereira-Conca, and K.-H. Schmidt, Nucl. Instrum. Methods A **478**, 493 (2002).

[20] T. Enqvist, W. Wlazło, P. Armbruster, J. Benlliure, M. Bernas, A. Boudard, S. Czajkowski, R. Legrain, S. Leray, B. Mustapha, M. Pravikoff, F. Rejmund, K.-H. Schmidt, C. Stéphan, J. Taïeb, L. Tassan-Got, and C. Volant, Nucl. Phys. **A686**, 481 (2001).

[21] D. Henzlova, Ph.D. thesis, Czech Technical University Prague, Faculty of Nuclear Science and Engineering (2006).

[22] K.-H. Schmidt, E. Hanelt, H. Geissel, G. Münzenberg, and J.-P. Dufour, Nucl. Instrum. Methods A **260**, 287 (1987); also http://www.gsi.de/charms/amadeus.htm.

[23] C. J. Benesh, B. C. Cook, and J. P. Vary, Phys. Rev. C **40**, 1198 (1989).

[24] D. J. Morrissey, Phys. Rev. C **39**, 460 (1989).

[25] A. S. Goldhaber, Phys. Lett. **B53**, 306 (1974).

[26] E. Hanelt, A. Grewe, K.-H. Schmidt, T. Brohm, H.-G. Clerc, M. Dornik, M. Fauerbach, H. Geissel, A. Magel, G. Münzenberg, F. Nickel, M. Pfützner, C. Scheidenberger, M. Steiner, K. Sümmerer, B. Voss, M. Weber, J. Weckenmann, and C. Ziegler, Z. Phys. A **346**, 43 (1993).

[27] P. Napolitani, K.-H. Schmidt, A. S. Botvina, F. Rejmund, L. Tassan-Got, and C. Villagrasa, Phys. Rev. C **70**, 054607 (2004).

[28] M. V. Ricciardi, A. V. Ignatyuk, A. Kelić, P. Napolitani, F. Rejmund, K.-H. Schmidt, and O. Yordanov, Nucl. Phys. **A733**, 299 (2004).

[29] M. de Jong, K.-H. Schmidt, B. Blank, C. Böckstiegel, T. Brohm, H.-G. Clerc, S. Czajkowski, M. Dornik, H. Geissel, A. Grewe, E. Hanelt, A. Heinz, H. Irnich, A. R. Junghans, A. Magel, G. Münzenberg, F. Nickel, M. Pfützner, A. Piechaczek, C. Scheidenberger, W. Schwab, S. Steinhäuser, K. Sümmerer, W. Trinder, B. Voss, and C. Ziegler, Nucl. Phys. **A628**, 479 (1998).

[30] T. Enqvist, P. Armbruster, J. Benlliure, M. Bernas, A. Boudard, S. Czajkowski, R. Legrain, S. Leray, B. Mustapha, M. Pravikoff, F. Rejmund, K.-H. Schmidt, C. Stéphan, J. Taïeb, L. Tassan-Got, F. Vivès, C. Volant, and W. Wlazo, Nucl. Phys. **A703**, 435 (2002).

[31] F. Rejmund, B. Mustapha, P. Armbruster, J. Benlliure, M. Bernas, A. Boudard, J. P. Dufour, T. Enqvist, R. Legrain, S. Leray, K.-H. Schmidt, C. Stéphan, J. Taïeb, L. Tassan-Got, and C. Volant, Nucl. Phys. **A683**, 540 (2001).

[32] C. Gaarde, Annu. Rev. Nucl. Part. Sci. **41**, 187 (1991).

[33] A. Kelić, K.-H. Schmidt, T. Enqvist, A. Boudard, P. Armbruster, J. Benlliure, M. Bernas, S. Czajkowski, R. Legrain, S. Leray, B. Mustapha, M. Pravikoff, F. Rejmund, C. Stephan, J. Taïeb, L. Tassan-Got, C. Volant, and W. Wlazło, Phys. Rev. C **70**, 064608 (2004).

[34] L. N. Andronenko, L. A. Vaishnene, A. A. Kotov, M. M. Nesterov, N. A. Tarasov, and V. Neubert, Fiz. Elem. Chastits At. Yadra **18**, 685 (1987); Sov. J. Part. Nuclei **18**, 289 (1987).

[35] A. S. Botvina, I. N. Mishustin, M. Begemann-Blaich, J. Hubele, G. Imme, I. Iori, P. Kreutz, G. J. Kunde, W. D. Kunze, V. Lindenstruth, U. Lynen, A. Moroni, W. F. J. Müller, C. A. Ogilvie, J. Pochodzalla, G. Raciti, Th. Rubehn, H. Sann, A. Schüttauf, W. Seidel, W. Trautmann, and A. Wörner, Nucl. Phys. **A584**, 737 (1995).

[36] P. Marmier and E. Sheldon, *Physics of Nuclei and Particles* (Academic Press, New York 1969), p. 36.

[37] J. P. Dufour, H. Delagrange, R. Del Moral, A. Fleury, F. Hubert, Y. Llabador, M. B. Mauhourat, K.-H. Schmidt, and A. Lleres, Nucl. Phys. **A387**, 157c (1982).

[38] R. J. Charity, Phys. Rev. C **58**, 1073 (1998).